Band structures of ^{131}Ce

Thesis submitted in accordance with the requirements of the University of Liverpool for the degree of Doctor in Philosophy

by

Mohammed Abdullah Alwaleedi

Oliver Lodge Laboratory

2013

Abstract

High-spin states have been studied in the neutron-deficent odd-N ^{131}Ce nucleus. The experiment was performed at Argonne Laboratory, USA, using the fusion evaporation reaction ^{100}Mo(^{36}S,5nγ). The beam of ^{36}S was produced by the Argonne Tandem Linac Accelerator System (ATLAS) to an energy of 165 MeV with a beam current of 5 pnA. The gamma ray coincidence data were recorded with GAMMASPHERE.

A detailed spectroscopic study of the ^{131}Ce nucleus has established two new band structures and extended some of the known bands to higher spin. Cranked Woods-Saxon calculations have been used to assign possible configurations for the newly found structures. Angular intensity-ratio measurements have been performed to gain information on the multipolarities of transitions in this nucleus.

In order to strengthen the suggested configuration for the ^{131}Ce bands a comparison was carried out between the experimental and theoretical B(M1)/B(E2) ratios of reduced transition probabilities. A large signature splitting in the negative-parity bands is discussed as evidence for non-axial nuclear shape which is induced by the core-polarisation effects of neutrons from the upper $h_{11/2}$ midshell.

.

This thesis is dedicated to my parents and wife

Acknowledgements

Firstly, I would like to thank my supervisors, Prof. P. J. Nolan and Dr. E. S. Paul, for allowing me to carry out this research at the University of Liverpool and for their support throughout my Ph. D. I also wish to acknowledge the Saudi government for funding my Ph. D studies.

I would like to thank the nuclear structure group for their help over all the years of my studies and also Ms. Janet Sampson and Dr. John Cresswell for their help in computing throughout this time.

Finally, I would like to say a special thank you to my parents, my wife (Amani) and my daughters for their support and love during my time at the University of Liverpool.

List of Figures

List of Tables

Contents

Chapter 1

Introduction

1.1 Introduction

The recent developments in heavy ion accelerators and gamma-ray spectrometer arrays, such as GAMMASPHERE, have facilitated the study of nuclear structure at high angular momentum. The high spin states of ^{131}Ce were populated using the ^{100}Mo(^{36}S,5nγ) fusion evaporation reaction carried out at the Argonne laboratory, USA. The beam of ^{36}S was produced by the ATLAS accelerator to an energy of 165 MeV with a beam current of 5 pnA. This beam bombarded two enriched self-supporting foils of ^{100}Mo each of which had a thickness of 600 μg/cm^2. GAMMASPHERE consisted of 101 Compton-suppressed Hyper-Pure Germanium Detectors, which were used to record γ-ray events. The total run time for this experiment was 18×8 hour shifts. A total of 3×10^9 events of fold $k \geq 7$ were recorded. The data were unfolded off-line into quadruple coincidence events and replayed into a 4-dimensional hypercube. The analysis was carried out using 4DG8R software. In this work two new strongly coupled bands have been found and the known bands have been extended to higher spin. Woods-Saxon cranking calculations are used to interpret the band structure, and measured B(M1)/B(E2) reduced transition probability ratios are compared with theory in order to support the configuration assignments. Angular intensity ratio measurements have been performed to gain information on the multi-

polarities of transitions in this nucleus. This thesis consists of the following chapters:
Chapter 2 : This chapter presents an introduction to the nuclear models related to the present study. The Shell Model, Nuclear deformation and the Nilsson Model are discussed. In addition to that, this chapter discusses nuclear rotation, the Cranked Shell Model and some nuclear aspects which are relevant to this study.

Chapter 3 : In this chapter, the experimental techniques such as Heavy Ion Evaporation reactions, the GAMMASPHERE array and the angular intensity ratios, are discussed in detail.

Chapter 4 : The results of this study are displayed in two sections; namely, the negative parity bands and the positive parity bands. The level scheme, the spectra, gamma-ray energies, relative intensities, angular intensity ratio measurements and spin/parity for all bands are shown in detail.

Chapter 5 : This chapter contains the interpretation of all bands in ^{131}Ce. A comparison with Cranked Woods-Saxon calculations and theoretical B(M1)/ B(E2) ratios was carried out to confirm and assign the possible configuration for the known and new structures respectively.

Chapter 2

Theory

2.1 Introduction

In order to understand the nucleus, which is a very complex system, and to gain some information about its structure, it must be examined under extreme conditions (i.e. high angular momentum). In addition to that, a knowledge of nuclear theory is required. Over the past century, many attempts have been made and various models have been improved but no one has yet offered a full understanding of the nucleus. One of the first models is the liquid drop model (LDM) by Weizsäcker [1]. Despite the success of this model in predicting the bulk properties of the nucleus, it fails to explain the existence of stable nuclei at proton or neutron numbers of :

$$N, Z = 2, 8, 20, 28, 50, 82 \text{ and } 126. \tag{2.1}$$

so, another type of model is needed. Hence, this chapter will discuss this in detail.

2.2 Shell Model

Following the failure of the liquid drop model to explain the shell type structure in the nucleus, the shell model was developed. The idea of this model is to treat the nucleons in a similar manner to that of electrons of an atom. In this model, the nucleus is

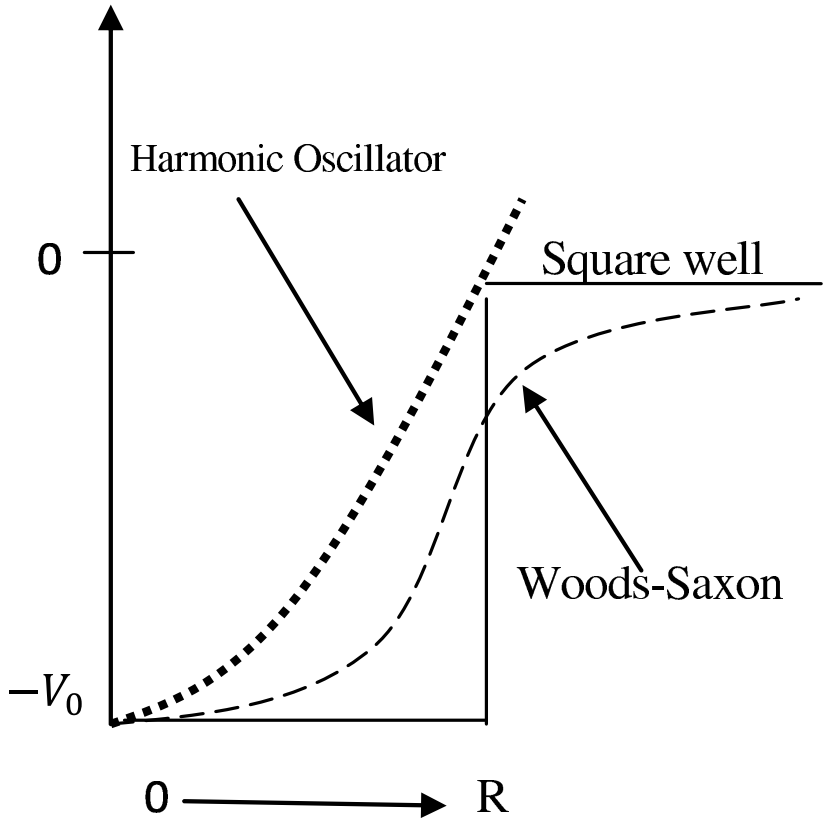

Figure 2.1: Comparison between three potential wells used to model the nuclear potential.

considered to be a spherical system, where each nucleon moves independently within a potential. This potential is produced by the other nucleons. The nuclear Hamiltonian H, which describes this system, is defines as [2] :

$$H = \sum_i T_i + \sum_i V(r_i). \tag{2.2}$$

It consists of the average potential plus the sum of the individual kinetic energies of all of the independent nucleons. Various attempts have been made to model the observed nuclear energy levels. Three of the most used potential wells, are illustrated in Figure 2.1, and described in the following section.

2.3 Nuclear Potential

The simplest way to describe the nuclear potential is the square well potential. This potential has a sharp edge as shown in Figure 2.1. It is not a good approximation for the nuclear potential because the latter does not have a sharp edge and this provides an unrealistic description of the interaction at the surface of the nucleus. This potential can be defined as:

$$V(r) = \begin{cases} -V_o & r < R \\ 0 & r > R \end{cases} \tag{2.3}$$

where r is the distance from the centre of the nucleus, R is the nuclear radius and V_o is the depth of the well. As a result of using this potential the magic numbers are

$$2, 8, 18, 20, 34, 40 \text{ and } 58. \tag{2.4}$$

Hence, this potential reproduced the first two magic number correctly [3]. The second method used to describe the nuclear potential is the harmonic oscillator. This can be written as [4] :

$$V_{HO}(r) = -V_o + \frac{1}{2}M\omega^2 r^2 \tag{2.5}$$

where V_o is the depth of the well, M is the nucleon mass and ω is the frequency of the simple harmonic motion of the particle. Solving the Schrödinger equation can give a set of energy levels:

$$E_N = \left(N + \frac{3}{2}\right)\hbar\omega \tag{2.6}$$

each N shell has a degenerate group of different l levels, given by $l \leq N$, where l is the orbital angular momentum quantum number which is restricted to odd (or even) values when N is odd (or even), and can be occupied by a maximum of (N+1)(N+2) nucleons. The parity of the levels is given by :

$$\pi = (-1)^N. \tag{2.7}$$

The harmonic oscillator potential reproduced only the first three magic numbers correctly. Therefore, another way is needed to reproduce the correct magic numbers.

The third attempt to introduce a more realistic potential is the Woods-Saxon potential. It can be seen from Figure 2.1 that this potential is an intermediate version of the harmonic oscillator and the square well potential. It can be written as [5] :

$$V(r) = \frac{-V_o}{1 + \exp[(\mathrm{r} - \mathrm{R_o})/\alpha]} \tag{2.8}$$

where V_o is the potential depth, R_o is the nuclear radius and α is the surface diffuseness. This potential can produce the first three magic numbers. Consequently, a further modification is needed in order to make it valid for heavier nuclei. This modification is the spin-orbit term which is explained in detail in section 2.4.

2.4 Spin-Orbit Coupling

The spin-orbit interaction is added to the nuclear potentials in order to reproduce the correct magic numbers [6, 7]. In this interaction, the orbital angular momentum and intrinsic spin are coupled to give the total angular momentum j:

$$\vec{j} = \vec{l} + \vec{s}. \tag{2.9}$$

The spin-orbit coupling potential can be written as:

$$V_{so} = f(r)\vec{l}.\vec{s} \tag{2.10}$$

where $f(r)$ is the strength of interaction. This interaction splits the energy levels into two components, one of them $j = l + 1/2$ is lower in energy than the $j = l - 1/2$ and each state can contain $2j + 1$ nucleons. This leads to the occurrence of what are called intruder states. As a result of that, the correct magic numbers were reproduced. Figure 2.2 shows the single particle energy levels of the Wood-Saxon potential.

2.5 Nuclear Deformation

The basic shell model assumes that the average nuclear potential is a spherically symmetric one. This assumption succeeded for the description of nuclei near the

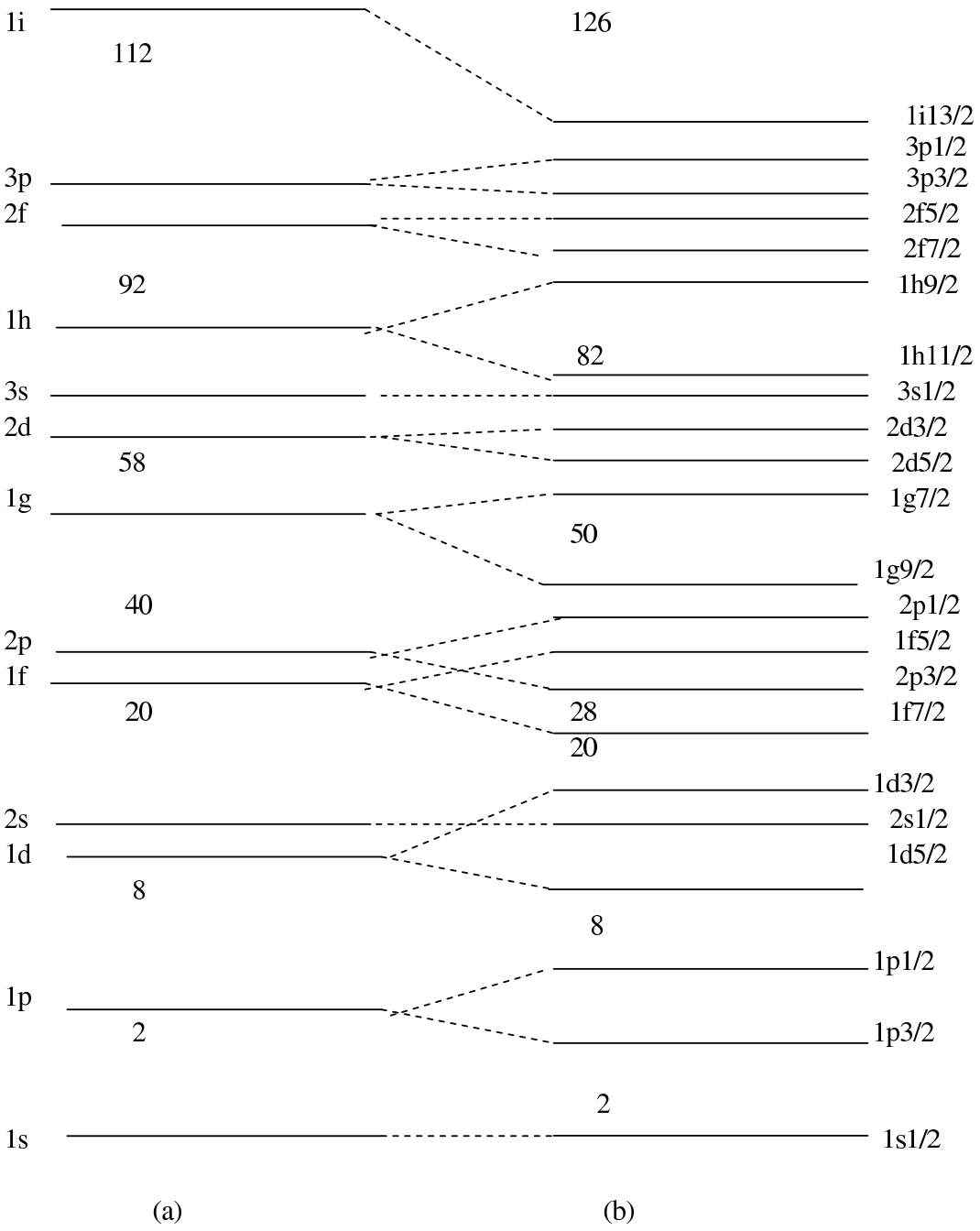

Figure 2.2: The level energy produced by (a) Woods-Saxson potential, (b) Wood-Saxon with spin-orbit coupling.

closed shells. Despite this success experimental evidence has proven the existence of stable deformed shapes in the nuclei between closed shells. This evidence includes rotational bands and large quadrupole moments. Therefore, there is a need for a deformed potential rather than a spherical one to describe such nuclei. The shape of a deformed nucleus can be described by defining the nuclear radius $R(\theta, \phi)$ from the centre of the nucleus to a point on the surface, using spherical polar coordinates :

$$R(\theta, \phi) = R_o \left(1 + \sum_{\lambda=0}^{\infty} \sum_{\mu=-\lambda}^{\lambda} \alpha_{\lambda\mu} Y_{\lambda\mu}(\theta, \phi) \right) \tag{2.11}$$

where R_o is the radius of a sphere and is equal to $r_o A^{1/3}$, $\alpha_{\lambda\mu}$ is the coefficient of multipole expansions and $Y_{\lambda\mu}(\theta, \phi)$ are the spherical harmonics. The coefficient $\alpha_{\lambda\mu}$ for quadrupole deformation ($\lambda = 2$) can be written in terms of the deformation parameters β_2 and γ as [8] :

$$\alpha_{20} = \beta_2 \cos\gamma \tag{2.12}$$

$$\alpha_{22} = \alpha_{2-2} = \frac{1}{\sqrt{2}} \beta_2 \sin\gamma \tag{2.13}$$

where the β_2 parameter is proportional to the elongation of the axially symmetric shape, and γ is the triaxiality parameter. For quadrupole deformations, the axially symmetric collective shapes are prolate at $\gamma = 0°$ or oblate at $\gamma = -60°$, while the non collective shapes can be seen at $\gamma = -120°$ and $60°$ respectively. The triaxial shapes of the deformed nucleus along the z-axis can be observed in the sector of the (β_2,γ) plane, when triaxial parameter changes between angles $0° < \gamma < 60°$. Figure 2.3 shows the different shapes in terms of deformation parameters (β_2,γ) [9].

2.6 The Anisotropic Harmonic Oscillator Potential

Deformation is usually introduced along the z-axis (i.e. x = y $\neq$z) where the nucleus is only axially symmetric about the z-axis. For a deformed nucleus, the Anisotropic

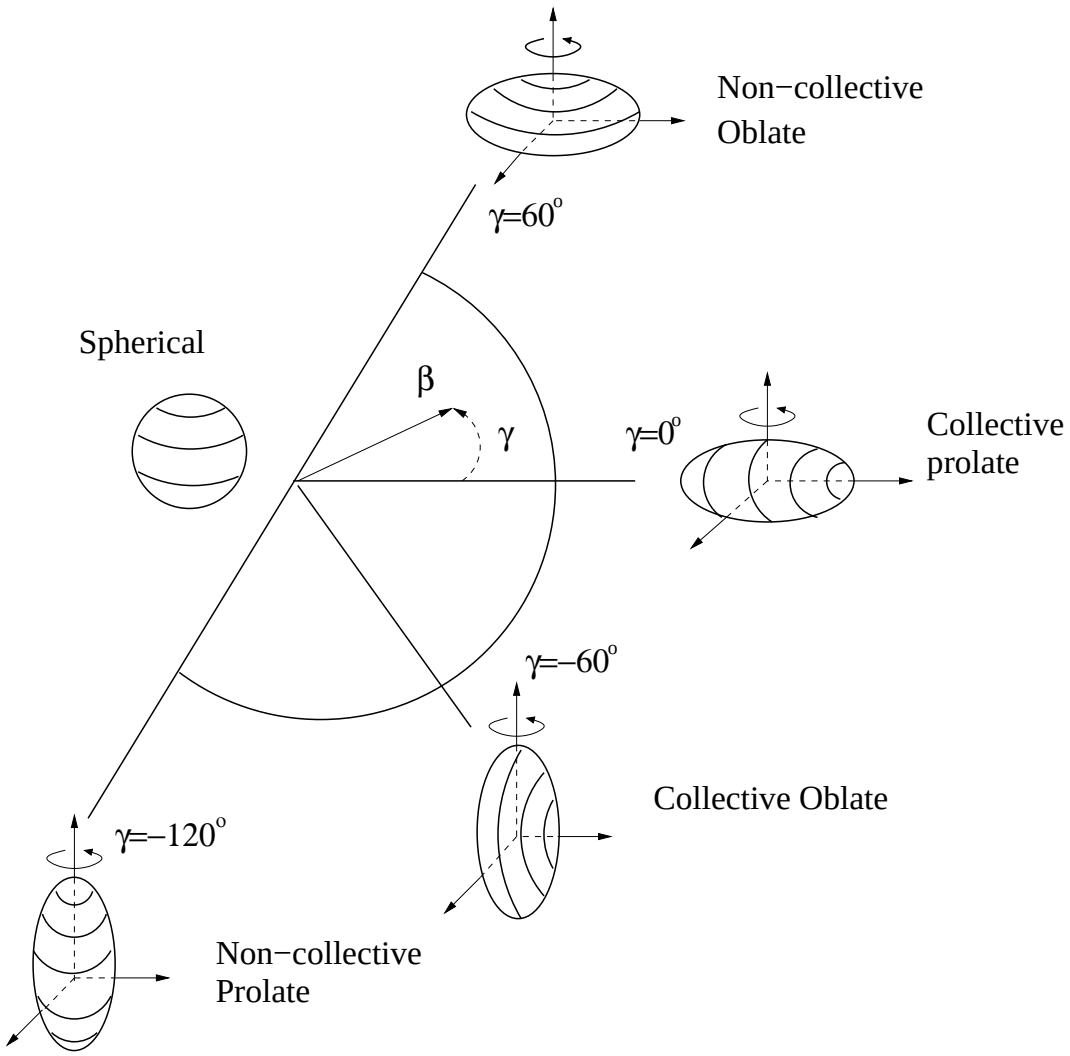

Figure 2.3: The Lund convention for describing quadrupole shapes [9].

Harmonic Oscillator (AHO) potential can be written as [10] :

$$V_{AHO} = \frac{1}{2}M\Big[\omega_{\perp}^2(x^2+y^2)+\omega_z^2 z^2\Big] \tag{2.14}$$

where $\omega_{\perp}$ and ω_z represent the frequencies of the simple harmonic motion in the direction perpendicular and parallel to the symmetry axis respectively. Anisotropy is achieved by the difference between $\omega_{\perp}$ and ω_z These frequencies can be introduced in terms of the deformation parameter δ as :

$$\omega_z \approx \omega_0\Big[1-\frac{2}{3}\delta\Big] \tag{2.15}$$

$$\omega_x = \omega_y = \omega_{\perp} \approx \omega_0\Big[1+\frac{1}{3}\delta\Big]. \tag{2.16}$$

with $\omega_0^3 = \omega_{\perp}^2\ \omega_z$ for volume conservation. The harmonic oscillator quantum ω_0 can be deduced from :

$$\hbar\omega_0 = 41A^{-1/3}\Big[1 \pm \frac{N-Z}{3A}\Big](\text{MeV}), \tag{2.17}$$

where the positive sign is used for neutrons and the negative sign for protons. In order to introduce the deformed potential in terms of the deformation ε_λ parameters and the angle of the stretched coordinates Nilsson transformed the problem of the anisotropic harmonic oscillator potential to stretched coordinates (ξ, η, ζ). Thus, the potential for the $\lambda = 2$ case can be written as [12, 13] :

$$V_{AHO} = \frac{1}{2}\hbar\omega(\varepsilon_2)\rho^2[1-\frac{2}{3}\varepsilon_2 P_2(\cos\theta_t)] \tag{2.18}$$

where ρ is a term relating to the sum of the stretched coordinates, θ_t is the angle in the stretched coordinates and ε_2 is the quadrupole deformation in the stretched coordinates, which is approximately equal to $0.95\beta_2$.

2.7 The Nilsson Model

The Nilsson model describes the single-particle states of deformed nuclei. It is based on a modified version of the anisotropic harmonic oscillator potential. The Nilsson potential or the modified harmonic oscillator (MHO) can be written as :

$$V_{MHO} = V_{AHO} - \kappa\hbar\omega\Big[2l.s + \mu(l^2 - \langle l^2\rangle_N)\Big] \tag{2.19}$$

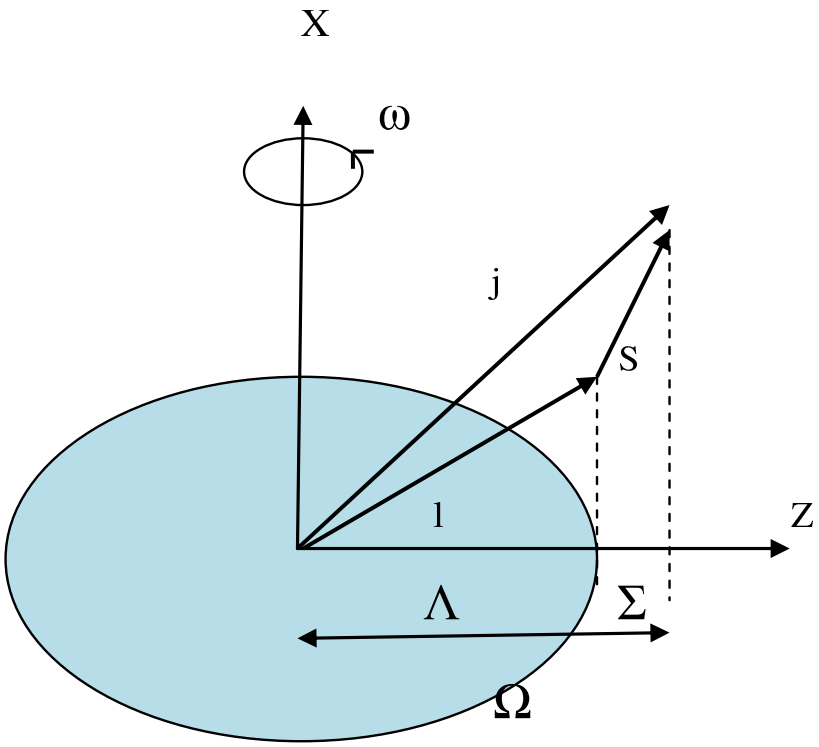

Figure 2.4: An illustration of the relationship between Nilsson quantum numbers.

where κ and μ are adjustable coupling parameters which are obtained by fitting to the experimental energy levels. These parameters are different for each major oscillator shell. The second term in the Nilsson potential is the spin-orbit coupling, which is explained in section 2.4. The last term was added to flatten the potential well to be more accurate for describing the nuclear shape. The energy levels obtained by the Nilsson model are labelled using the form:

$$[Nn_z\Lambda]\Omega^\pi \tag{2.20}$$

where N is the oscillator shell number, n_z is the component of N along the symmetry axis (z-axis), Λ is the projection of orbital angular momentum on the symmetry axis, and Ω is the projection of the total angular momentum on the symmetry axis which can be written as

$$\Omega = \Lambda \pm \Sigma = \Lambda \pm 1/2 \tag{2.21}$$

where Σ is the projection of the spin on the symmetry axis. Finally, π is the parity of the state. These quantum numbers are illustrated in Figure 2.4.

Figures 2.5 and 2.6 show the single partical energy levels as a function of quadrupole deformation, ε_2, for neutrons and protons respectively. At $\varepsilon_2 \approx 0$ each spherical level is split into $(2j+1)/2$ levels and the shell closures appear as regions of low density. Levels with low Ω are lowered in energy at $\varepsilon_2 > 0$ that represent the prolate deformation and raised in energy for oblate deformation at $\varepsilon_2 < 0$. The only good quantum numbers are Ω and $\pi = (-1)^N$. The solid lines display the positive parity states and the dashed lines display the negative ones. As a consequence of the Pauli exclusion principle, levels with the same Ω and π quantum numbers can not cross but exchange their trajectories and characteristics at the crossing point.

2.8 Pairing

Pairing is a short-range interaction [14, 15] that is incorporated into the shell model in order to explain some of the nuclear properties. In this interaction, nucleons

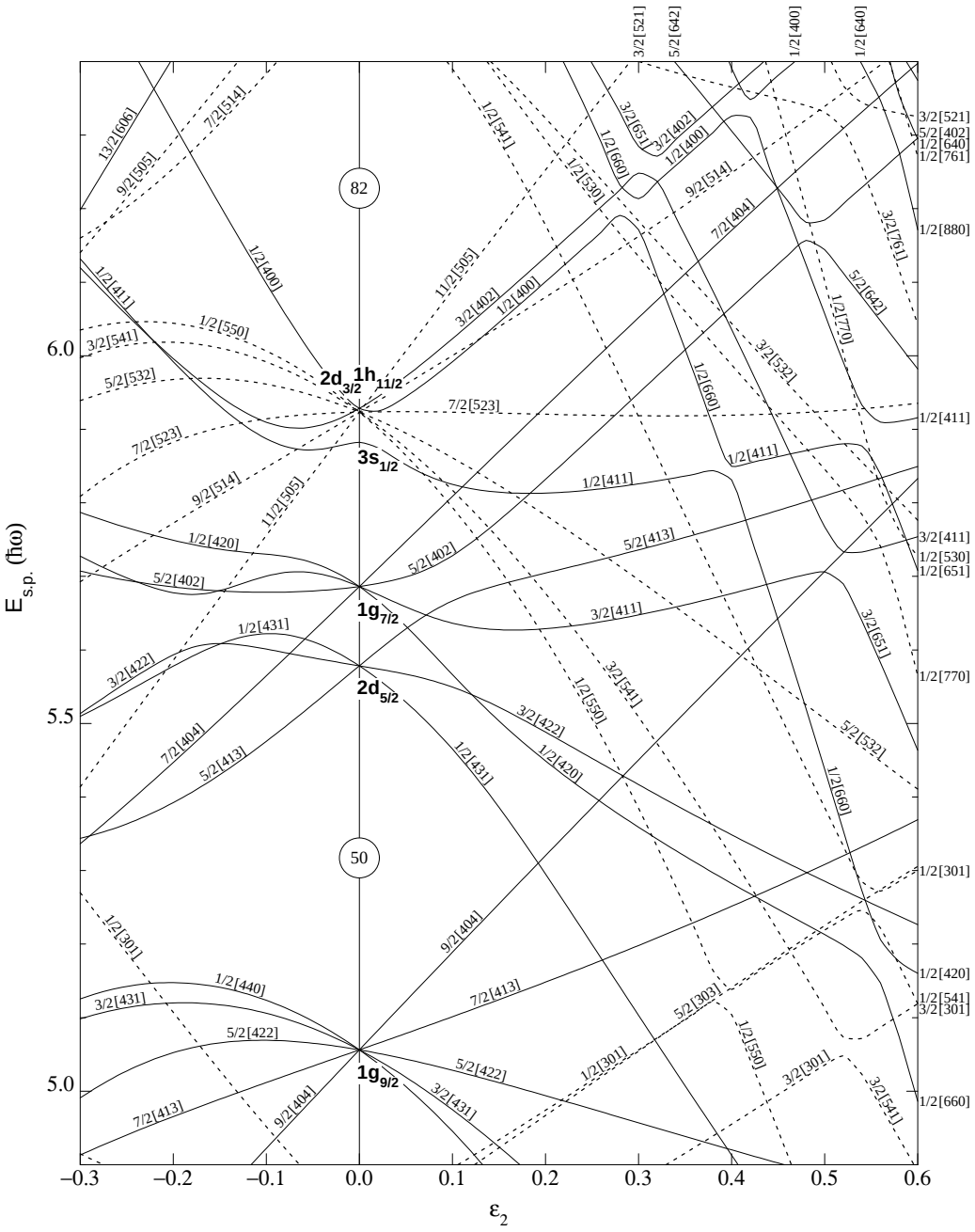

Figure 2.5: Nilsson diagram of single-neutron energies (50< N < 82) as a function of the quadruple deformation parameter ε_2.

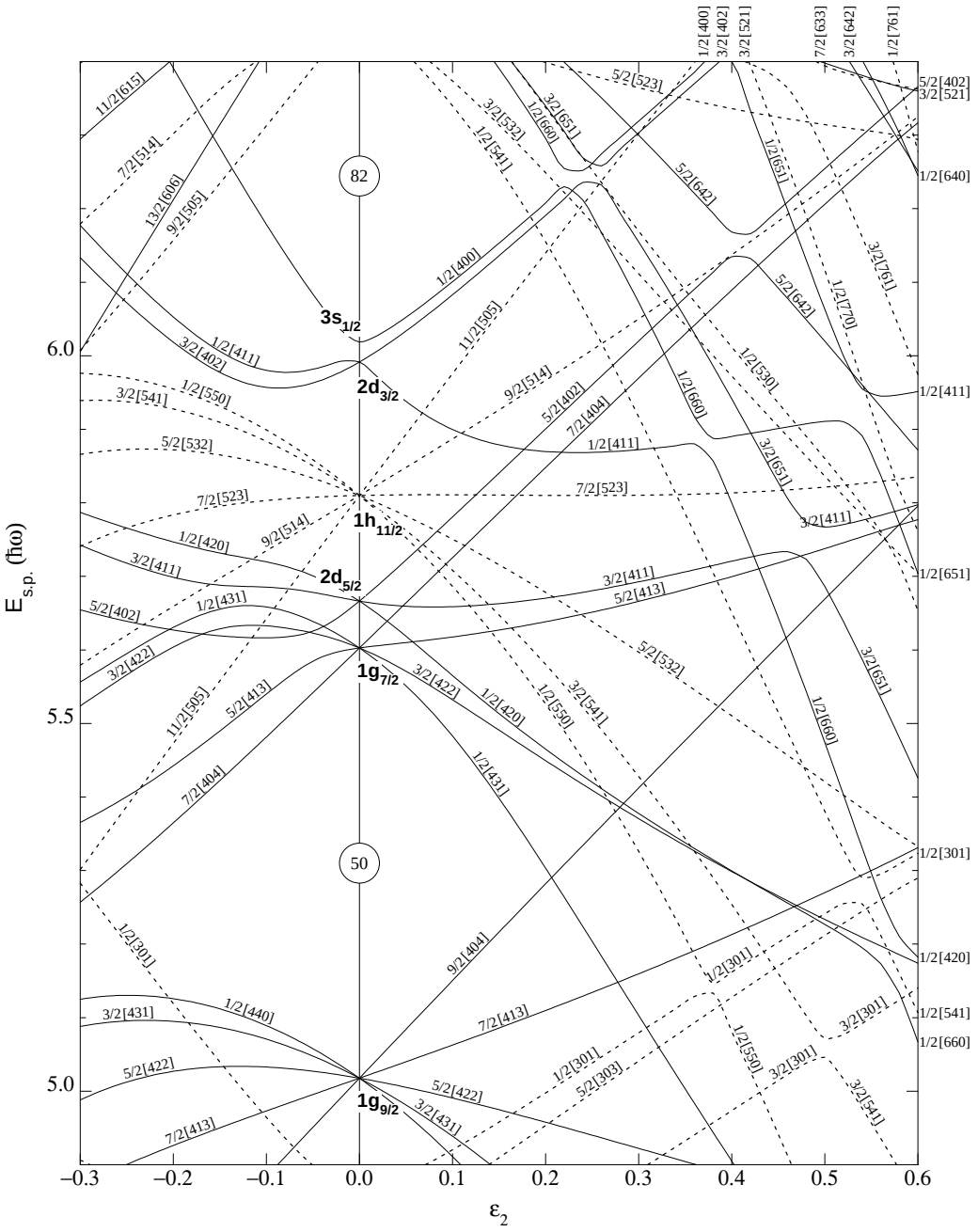

Figure 2.6: Nilsson diagram of single-proton energies (50< N < 82) as a function of the quadruple deformation parameter ε_2.

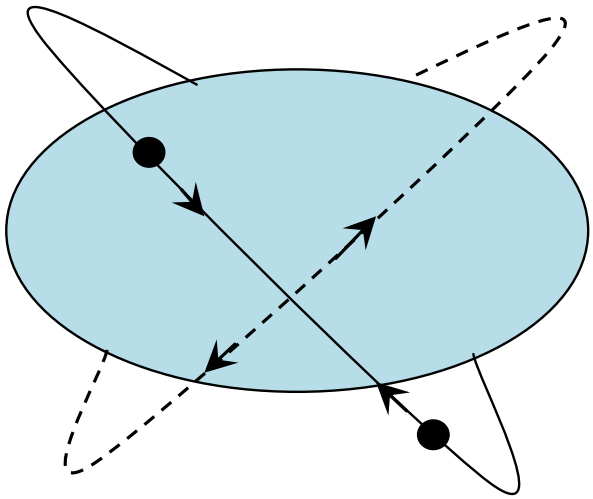

Figure 2.7: An illustration of paired nucleons orbiting in time-reversed orbits and scattering twice per orbit.

are coupled in pairs. This explains why even-even nuclei have a ground state with spin and parity of $I^{\pi} = 0^{+}$ and binding energies that are stronger than even-odd nuclei. Further experimental evidence for pairing is that the nuclear moment of inertia is smaller than the expected value of a rigid-body at low spin due to the creation of surface fluidity. Other experimental observations that can be explained in terms of pairing are the appearance of an energy gap of 1.5 MeV in non-collective excitation energy in even-even nuclei and even-even nuclei near to closed shells exhibit vibrational states which cannot be explained in terms of rotation or single-particle effects. The pairing can be described as two nucleons occupying the same orbital with the same quantum numbers but, in order to satisfy the Pauli principle, they travel in opposite directions. Thus, the total angular momentum of the pair is zero [16]. They orbit in time reversed orbits and interact twice per orbit, where they scatter into another time reversed orbit as shown in Figure 2.7. The pairing interaction only occurs near the Fermi surface because there are no free energy levels available inside. As a result of this interaction, the nucleons spend a finite time above and below the Fermi surface so the scattering smears out the Fermi surface (see Figure 2.8). The scattering of pairs into different orbitals introduces the concept of quasiparticles,

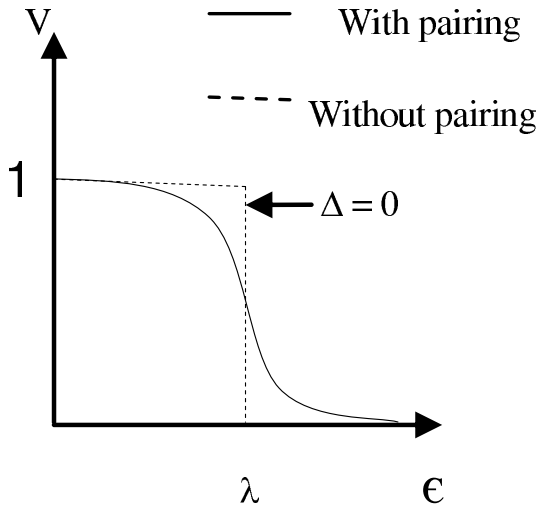

Figure 2.8: The effect of pairing on the Fermi surface

which describes the state as being occupied by either a particle or a hole. This can be defined by the orbit's probability of being occupied V_i^2 or unoccupied U_i^2. Therefore, the particle-hole excitation can be introduced by simultaneous creation and annihilation of quasiparticles. The quasiparticle energy of a state (i) is given by:

$$E_i = \sqrt{(\epsilon_i - \lambda)^2 + \Delta^2} \tag{2.22}$$

where, ϵ_i is the single-particle energy, λ is the Fermi energy and Δ is the pair gap which has different values for protons and neutrons due to the repulsive Coulomb interaction. For even-even nuclei, the ground state is the quasiparticle vacuum state and the lowest intrinsic excitations are two-quasiparticle excitations.

2.9 Nuclear Rotation

There are two modes in the nucleus that generate spin, namely, non-collective single particle excitation and collective rotation. These two modes will be discussed in this section.

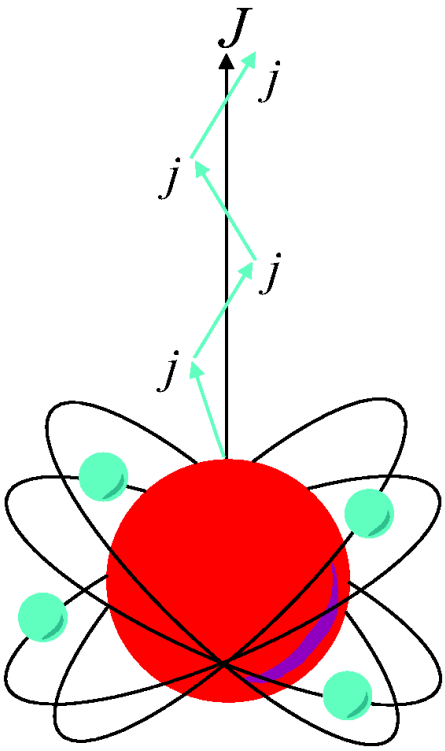

Figure 2.9: An illustration of Non-Collective Single Particle Excitation

2.9.1 Non-Collective Single Particle Excitation

Near to the closed shell regions where the shape of the nuclei are spherical or near spherical, these nuclei can generate spin by the non-collective mode in which the single particle aligns its spin along the rotation axis as seen in Figure 2.9. This mechanism gives rise to a large value of total angular momentum (J), if all valence nucleons are aligned, of the nucleus corresponding to the sum of the single particle contributions of the orbitals near to the Fermi surface. In addition to that, these nuclei cannot generate spin by the collective rotation mode because rotation about the symmetry axis is forbidden by quantum mechanical laws because the orientations of the intrinsic frame are indistinguishable. Nuclear excited states that are based on this mode of angular momentum generation are known as single particle excited states which can be observed in both spherical and deformed nuclei.

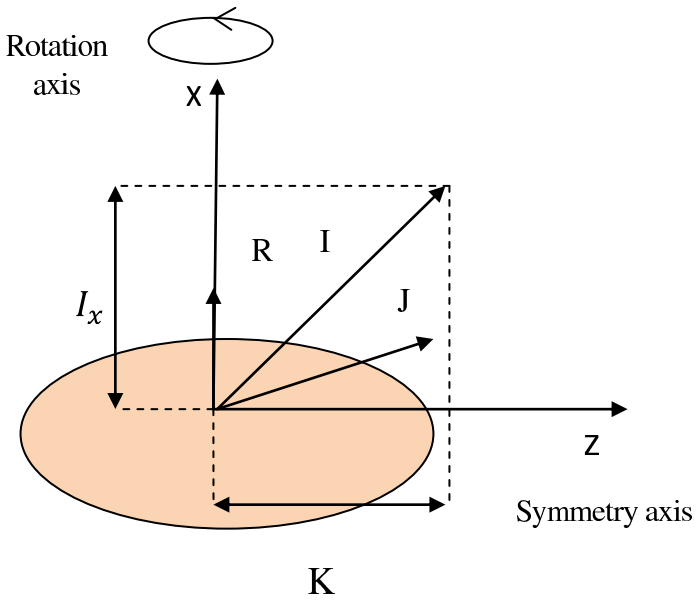

Figure 2.10: An illustration of nuclear rotation about an axis perpendicular to the symmetry axis in deformed nuclei

2.9.2 Collective Rotation

This mode of nuclear rotation can occur about an axis that is perpendicular to the symmetry axis in deformed nuclei (see Figure 2.10). This rotation is referred to the collective angular momentum of the core (R) and the sum of the intrinsic angular momentum of the unpaired valence nucleons which can be written as :

$$J = \sum_i j_i. \tag{2.23}$$

Thus (I) is given by :

$$I = R + J. \tag{2.24}$$

The rotational frequency of a deformed nucleus is related to the energy difference between successive states of a rotational band and is given by [17] :

$$\hbar\omega = \frac{dE}{dI_x} = \frac{E_\gamma}{2} \tag{2.25}$$

where I_x is the projection of the total angular momentum onto the rotation axis which is given by:

$$I_x = \sqrt{I(I+1)^2 - K^2}. \tag{2.26}$$

The collective rotation of the deformed nucleus results in a sequence of levels that are separated by a spin of 2 $\hbar$. This sequence is called a rotational band where the energy increases in proportion to I(I+1), as shown in the following equation:

$$E(I) = \frac{\hbar^2}{2\mathcal{J}} I(I+1) \tag{2.27}$$

where $\mathcal{J}$ is the moment of inertia, but, for a rotational band with K$\neq$0, the energy is given by:

$$E(I) = \frac{\hbar^2}{2\mathcal{J}} [I(I+1) - K^2]. \tag{2.28}$$

In order to describe the collective nuclear rotation, there are two moments of inertia [18]. Firstly, the kinematic moment of inertia :

$$\mathcal{J}^{(1)} = \frac{\hbar^2}{2} \Big[\frac{dE(I)}{dI_x} \Big]^{-1} = \hbar \frac{I}{\omega}. \tag{2.29}$$

Secondly, the dynamic moment of inertia :

$$\mathcal{J}^{(2)} = \hbar^2 \Big[\frac{d^2E(I)}{dI_x^2} \Big]^{-1} = \hbar \frac{dI}{d\omega}. \tag{2.30}$$

For experimental measurement, these moments of inertia are defined by:

$$\mathcal{J}^{(1)} = \hbar^2 \frac{2I-1}{E_\gamma}, \tag{2.31}$$

$$\mathcal{J}^{(2)} = \frac{4\hbar^2}{\Delta E_\gamma}, \tag{2.32}$$

where ΔE_γ is the energy difference between two adjacent gamma-rays. It is observed from the previous equation that $\mathcal{J}^{(2)}$ is not dependent on the spin of the level in the rotational band. However it is sensitive to the structural changes such as particle alignment effects.

2.10 Particle Rotor Coupling

There are two coupling limits for the valence nucleons (i.e. the nucleons outside the core of the paired nucleons) namely [19], the strong coupling limit or deformation alignment (DAL) and the weak coupling limit or rotation alignment (RAL). The strong coupling limit occurs at low rotational frequencies when the Coroilis force [20] is not strong enough to decouple the valence nucleons that are bound to the rotating deformed core of the nucleus. In this case, the deformed nuclear field affects the motion of the valence nucleons and couples them to the deformation of the core. The angular momentum of valence nucleons will be aligned with the symmetry axis (see Figure 2.11a) and K here which is the projection of J on the z-axis is a good quantum number, whereas, in the case of rotation alignment, the angular velocity of the rotating nuclear system becomes higher compared to the internal nucleon motion, the rotational frequency will increase as well as the Coriolis force which overcomes the deformed potential of the core and couples the nucleons motion to the rotation axis. Thus, the angular momentum will be aligned with the rotation axis (see Figure 2.11b). The energy of the Coroilis force is given as [21] :

$$E_{Cor} = \frac{\hbar^2}{\mathcal{J}} j.I \tag{2.33}$$

where j is the angular momentum of the valence nucleon and $\mathcal{J}$ is the moment of inertia of the system which is inversely proportional to the angular frequency of the nucleus. Consequently, high-j and low Ω orbitals are more sensitive to the Coriolis force and predicted to be aligned first. The transition from the deformation aligned coupling to the rotation aligned coupling introduced the concept of backbending in the rotational band [22, 23], (see section 2.14).

2.11 The Cranked Sell Model

The Cranked Sell Model (CSM) was introduced by Inglis [24, 25] and it developed [26] in order to describe the rotating nucleus about an axis perpendicular to the

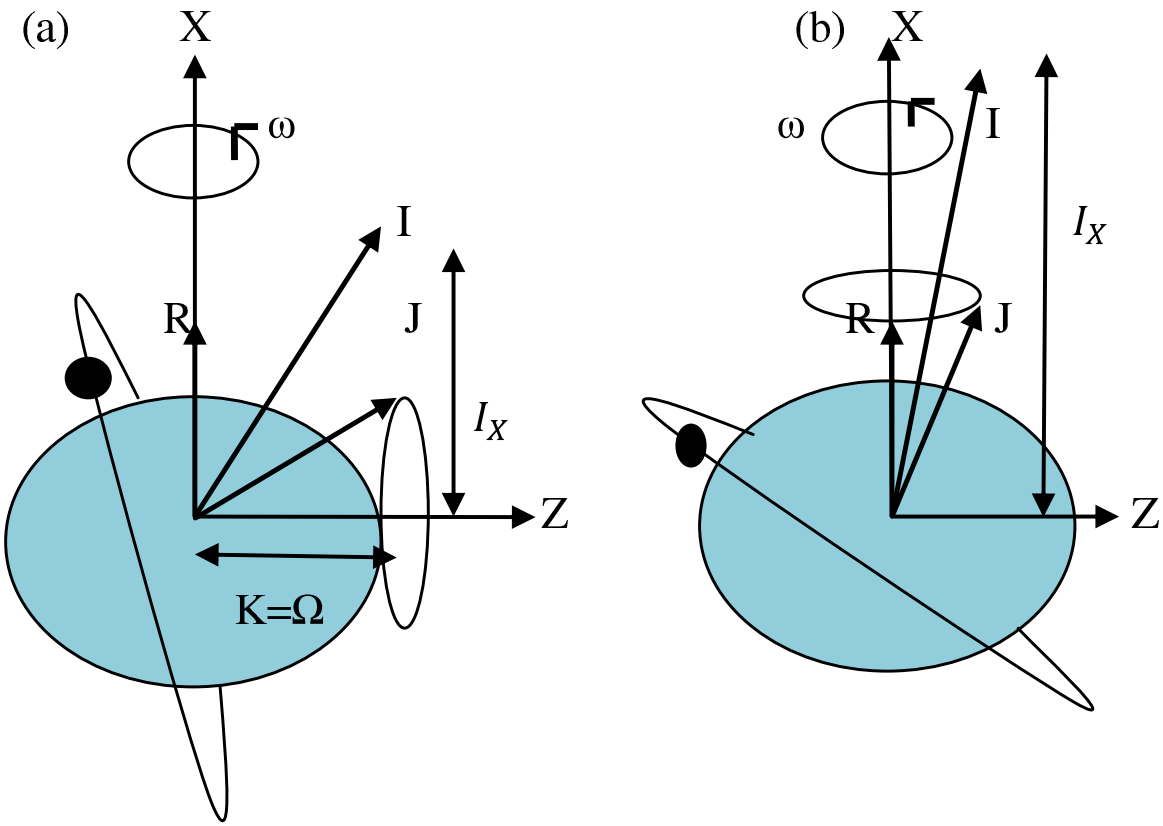

Figure 2.11: Particle rotor coupling scheme (a) Deformation aligned and (b) Rotational alignment.

symmetry axis. This model can describe the collective rotation and single particle excitation of a nucleus. This is achieved by introducing the cranking Hamiltonian for a single particle and adding up the single particle Hamiltonians. Furthermore, it treats nucleons as an independent particle moving in a rotating potential. So, the Hamiltonian is transformed into the rotating frame. The single particle cranking Hamiltonian can be written as :

$$h^{\omega} = h_{int} - \hbar\omega i_x \tag{2.34}$$

where the second term represents the effect of the centrifugal and Coroilis forces and i_x is the projection of the angular momentum on the rotational axis. The cranking Hamiltonian can be written as a sum of all the single particle Hamiltonians:

$$H^{\omega} = \sum h^{\omega} = H_{int} - \hbar\omega I_x \tag{2.35}$$

where H_{int} is sum of the single particle Hamiltonians in the intrinsic frame I_x is the sum of all single particle angular momentum onto the rotation axis. In this model the differential of the single particle Routhian energy,e', is related to the aligned angular momentum, i_x, by:

$$i_x = -\frac{de'}{d\omega} \tag{2.36}$$

Therfore, orbitals with large components of angular momentum aligned on the rotation axis are most affected by the rotation. The slope of Routhian is directly related to anguler moumentum of the orbital. This is useful in comparison to experimental data.

2.12 Parity and signature

In the axially symmetric quadrupole deformed nucleus rotating about an axis perpendicular to the axis of symmetry, the only two quantum numbers conserved under rotation are parity (π) and signature (α). The parity, is a reflection symmetry describing the behaviour of the spatial wave function after a reflection of all coordinates

Nucleus	α	I
even-A	0	0,2,4...
	1	1,3,5...
odd-A	$\frac{1}{2}$	$\frac{1}{2}, \frac{5}{2}, \frac{9}{2}$...
	- $\frac{1}{2}$	$\frac{3}{2}, \frac{7}{2}, \frac{11}{2}$...

Table 2.1: Allowed values of the signature number α and spin sequence I

through the origin, so, the parity quantum number is positive when the wavefunction is still positive after the inversion of all spatial coordinates or negative if the wavefunction changes sign after the inversion.
The other quantum number in this case is the signature which describes the invariance of the axially symmetric potentials with respect to a rotation of 180^o perpendicular to the symmetry axis. The rotation operator [27] is defined as:

$$R_x = \exp^{-i\pi i_x} . \tag{2.37}$$

The signature exponent quantum number (α) can be defined as:

$$r = \exp^{-i\pi\alpha} \tag{2.38}$$

where r is the eigenvalue of the rotation operator which introduced the signature quantum number. The relationship between the angular momentum and signature is defined as [27] :

$$I = \alpha \mod 2. \tag{2.39}$$

Thus, nuclei with even-A or odd-A result in the states summarised in table 2.1 Consequently, the Nilsson model states are split into two distinct signature partners. The degree of this splitting with increasing rotational frequency depends on the magnitude of the angular momentum projection onto the rotation axis I_x (see Figure 2.11). Thus, an orbit with high I_x and low Ω will be more affected. Finally, the cranking levels are only labelled by parity and signature (see Figure 2.12).

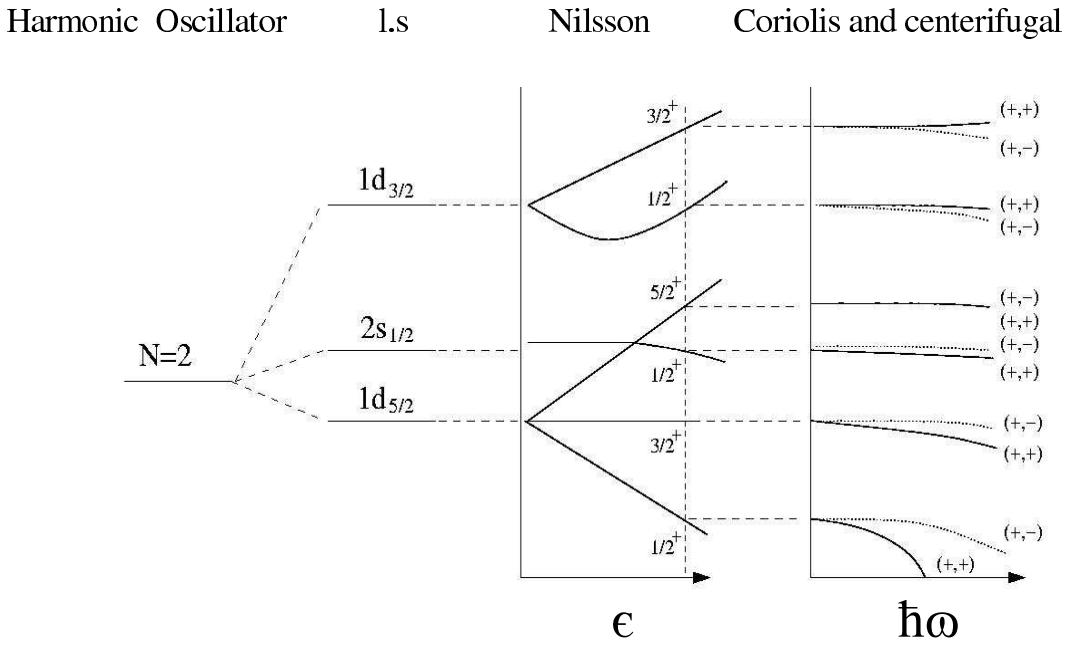

Figure 2.12: Schematic energy levels for shell model states generated by various nuclear potentials.

2.13 Cranked Shell Model Calculations

The cranked shell model calculations have been performed for ^{131}Ce with average deformation parameters as follows, quadrupole deformation parameter ($\beta_2 = 0.218$), hexadecapole deformation parameter ($\beta_4 = -0.023$) and the triaxiality parameter ($\gamma = 0°$) as illustrated in Figure 2.13. These parameters were obtained from total-Routhian surface (TRS) calculations [54, 56]. This figure shows the quasiparticle level energies e' in the rotating frame (Routhians) against the rotational frequency $\hbar\omega$. The Nilsson quantum numbers $[Nn_z\Lambda]\Omega^\pi$ can be used to label the quasiparticle levels at $\hbar\omega = 0$. When the rotating frequency increases, the Nilsson states split into two distinct levels, as explained in the previous section. At this point, the levels are identified by the remaining quantum numbers parity and signature (π, α) as follows: the solid lines represent the orbital with $(+, +1/2)$, the dotted lines represent the orbital with $(+, -1/2)$, the dot-dashed lines represent the orbital with $(-, +1/2)$ and the dashed lines represent the orbital with $(-, -1/2)$. The convention used to label

Neutrons		protons	
symbol	$(\pi, \alpha)_n$	symbol	$(\pi, \alpha)_n$
a	$(+, +1/2)_1$	A	$(+, +1/2)_1$
b	$(+, -1/2)_1$	B	$(+, -1/2)_1$
c	$(+, +1/2)_2$	C	$(+, -1/2)_2$
d	$(+, -1/2)_2$	D	$(+, +1/2)_2$
e	$(-, -1/2)_1$	E	$(-, -1/2)_1$
f	$(-, +1/2)_1$	F	$(-, +1/2)_1$
g	$(-, -1/2)_2$	G	$(-, -1/2)_2$
h	$(-, +1/2)_2$	H	$(-, +1/2)_2$

Table 2.2: This table shows the convention used to label the neutrons levels (small letters) and protons levels (capital letters).

the quasiparticles levels in this work are shown in Table 2.2.

There are some interesting features related to the cranked shell model calculations, as shown in Figure 2.13, as follows. Firstly, the theoretical gain in alignment can be calculated from the slopes of the interacting levels. Secondly, the strength of the interaction can provide information about band crossing, whether it is a backbend or upbend. In a backbend the distance between the interacting levels is smaller than that in the upbend. Furthermore, the splitting at a definite value of rotational frequency between levels with the same parity and opposite signature occurs due to the breaking of the time reversed orbit. Moreover, each level has a reflected level through $e' = 0$ but with an opposite signature. In addition, the quasiparticle levels with the same parity and signature do not cross but exchange their characters at this point where the interaction occurs between these levels. Finally, if one of the interacting levels is occupied by a particle, the crossing can not take place, which means that the particle blocks this level.

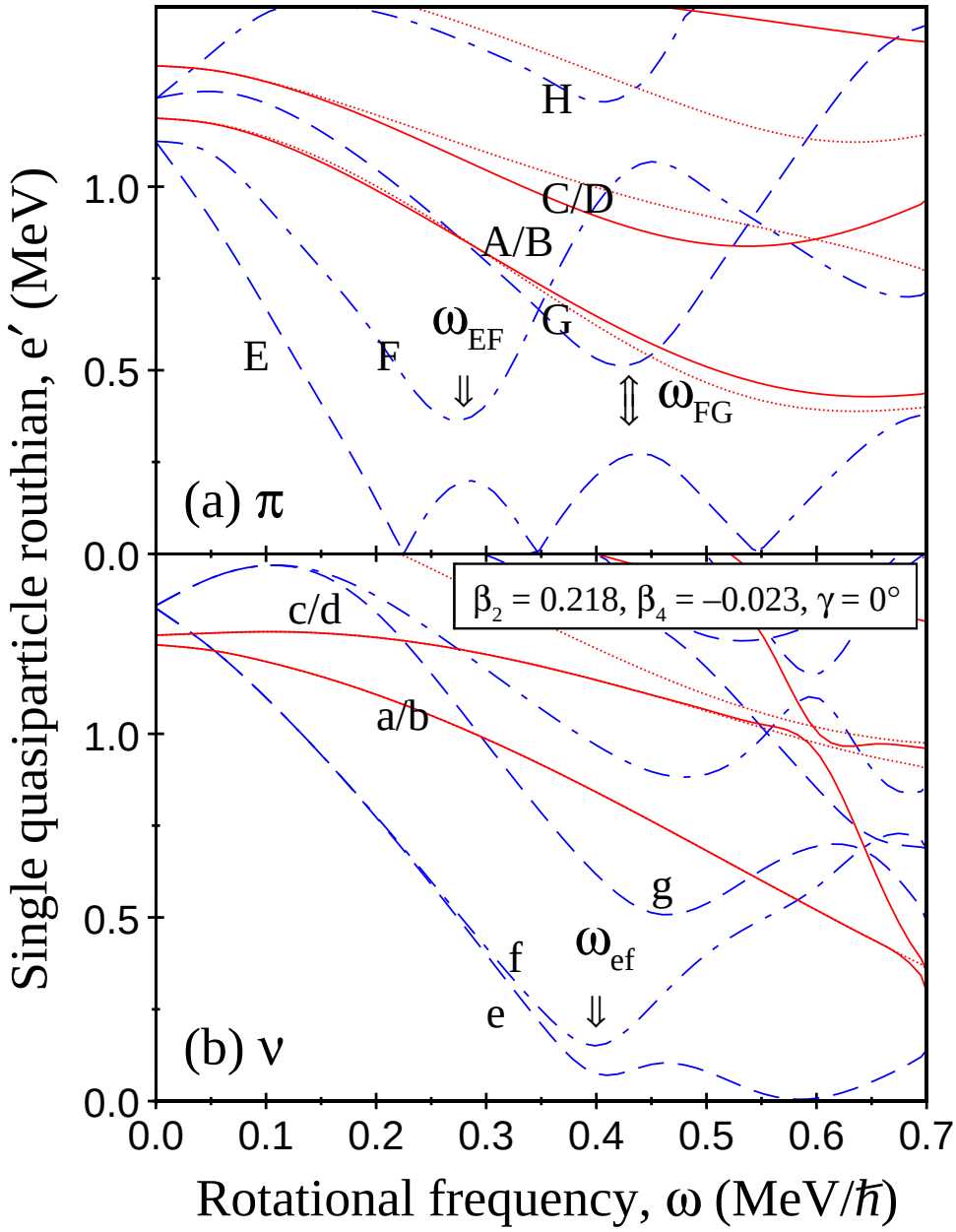

Figure 2.13: Cranked Shell Model Calculation for (a) protons and (b) neutrons.

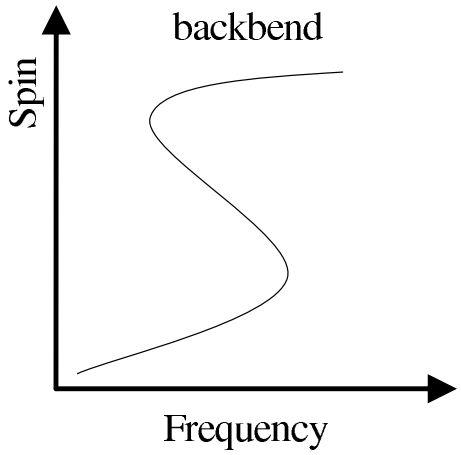

Figure 2.14: The spin as a function of rotational frequency showing the backbend

2.14 Backbending

The effect known as backbending can be interpreted as the crossing of two bands based on different intrinsic configurations. This crossing occurs when the Coriolis force becomes large enough to overcome the pairing force between a specific pair of coupled nucleons. This results in the nucleons aligning their angular momentum with the rotational axis. At low spin (typically around $12\hbar$ in even-A nuclei), the sequence corresponds to the ground state band (G band), whereas at higher spin (higher than $12\hbar$ in even-A nuclei), the Coriolis force become strong enough to break a pair of the valence nucleons in the time reversed orbits, and it becomes energetically favourable for the nucleus to form the next excited state by aligning their angular momentum with the rotational axis. This leads to a slowing down of the nuclear rotational frequency see Figure 2.14. The next sequence (S band) corresponds to a rotational band based on the aligned pair and has a higher moment of inertia than the ground state band.

Chapter 3

Experimental Techniques

3.1 Introduction

This chapter describes the experimental techniques used to produce nuclei at a high excitation energy and spin for spectroscopic studies of gamma-rays. It will discuss the Heavy-Ion Fusion Evaporation reaction, the gamma-ray decay, developments of high resolution gamma-ray detectors, the GAMMASPHERE array, and angular intensity ratio measurements.

3.2 Heavy Ion Fusion Evaporation Reaction

The most efficient reaction in order to study nuclear structure at high spin is the Heavy-Ion Fusion Evaporation reaction. This reaction populates states at a high angular momentum with sufficient energy and cross-section. It involves a heavy-ion accelerated beam as a projectile bombarding a target in order to form the compound nucleus. A very wide range of nuclei can be reached with considerable selectivity. The incident heavy ions in the beam fuse with the target to form the compound nucleus. This happens if the impact parameter (b) is small enough to ensure a complete fusion between the target and projectile but large enough to transfer a large amount of angular momentum (see Figure 3.1). The incident beam should have sufficient

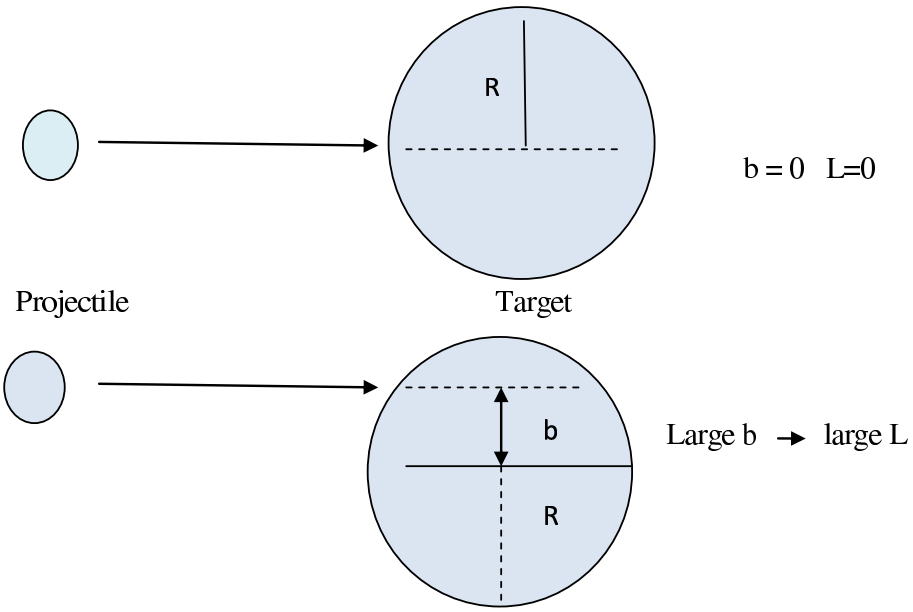

Figure 3.1: A Schematic representation showing the effect of the impact parameter b on the transferred angular momentum to the compound nucleus.

energy to overcome the Coulomb barrier which is defined as [28] :

$$E_{CB} = \frac{Z_p Z_t e^2}{4\pi\epsilon_o r}\text{MeV} \tag{3.1}$$

where r can be written as :

$$r = 1.2(A_p^{1/3} + A_t^{1/3})\text{fm} \tag{3.2}$$

where Z_p, A_p and Z_t, A_t are the atomic and mass number of the projectile and target nuclei. This mechanism imparts the largest angular momentum into the compound nucleus. The energy of the projectile is completely shared among the target nucleons. In this case the composite system loses all memory of the process of formation [29]. So, the decay process is independent of the process of formation. The compound nucleus decays firstly by particle evaporation. In this stage, it decays by neutron emission because there is no opposing Coulomb barrier, so the emission of neutrons is dominant, but proton and alpha emission also competes. The particle evaporation will carry away a large amount of energy but little angular momentum. Below the

particles threshold, the de-excitation then has to proceed via a statistical cascade, high energy dipole (E1) transitions, removing a large amount of energy but very little angular momentum, in addition to the collective cascade, which removes angular momentum via collective (E2) transitions. The previous two ways contribute to the unresolved background region. When the system is about 2-3 MeV from the yrast line, the level with the lowest energy at each spin, the density of states is low enough for discrete gamma-rays to be emitted. These gamma-rays remove large amounts of angular momentum and energy, then the nucleus reaches its ground state [30]. Figure 3.2 illustrates the decay of the compound nucleus following the Heavy-Ion evaporation reaction.

3.3 Heavy-Ion Beam Production

The incident beam must have sufficient kinetic energy to overcome the repulsion force of the Coulomb barrier by the target nucleus, in order to create the compound nucleus via the Heavy-Ion fusion evaporation reaction. In the present experiment the beam of ^{36}S atoms was produced, by the ATLAS accelerator, to an energy of 165 MeV with beam current of $\sim$ 5 pnA. This beam bombarded two enriched self-supporting foils of ^{100}Mo, each of which has a thickness of 600 μg/cm^2. GAMMASPHERE consisting of 101 Compton-Suppressed Hyper-Pure Germanium Detectors was used to record gamma-ray events. See section 3.10

3.4 Gamma Decay

A Gamma ray is a form of electromagnetic radiation which provides information about the energy difference between initial (E_i) and the final (E_f) states. The emitted gamma-ray would be the difference in energy between these states (i.e. $E_\gamma = E_i - E_f$). The decay of the gamma-ray depends on the conservation laws and the selection rules whereby one can measure the angular momentum or spin, excitation energy and parity. The character of the electromagnetic radiation of the emitted gamma-rays

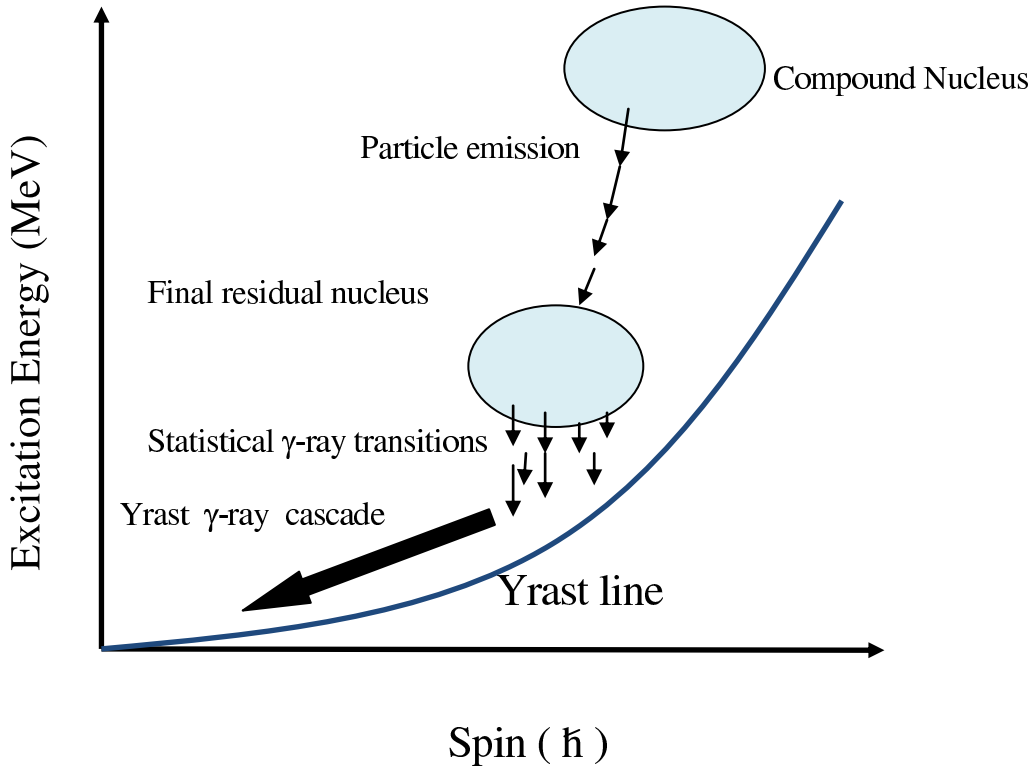

Figure 3.2: Schematic representation of the de-excitation of the compound neucleus.

is constrained by conservation of angular momentum and parity between initial and final excited states [3] :

$$\mid I_i - I_f \mid \leq L \leq I_i + I_f \tag{3.3}$$

where I_i, I_f are the spin of the initial and final states respectively and L is the multipole order of the emitted radiation. For stretched transitions ($L = \Delta I$). The change of parity between the initial and final states defines the electromagnetic nature of multipole orders of the emitted gamma-rays states as follow:

$$\Delta\pi(EL) = (-1)^L \tag{3.4}$$

$$\Delta\pi(ML) = (-1)^{L+1} \tag{3.5}$$

where $\Delta\pi(EL)$ and $\Delta\pi(ML)$ are the change of parity for electric transitions and magnetic transitions, respectively. This means that, the transitions between states of the same parity are of the even multipole order electric transitions and of the odd multipole order magnetic transitions (M1, E2, M3, E4,..), on the other hand transitions between the states of different parity are of the odd multipole order electric transitions and of the even multiple order magnetic transitions (E1, M2, E3, M4,...).

3.5 Semiconductors Detectors

The de-excitation process emits gamma-rays which are detected by measuring the interaction between the gamma-ray with the detector material. Semiconductors are used as detectors, since electron-hole pairs are created when the radiation travels through the semiconductor crystal. In order to collect the created charge the crystal is located between two electrodes. The ionisation energy in germanium, the energy required for producing one electron-hole pair, is very small $\approx$ 2.9 eV compared with a scintillator $\approx$ 300 eV. Thus, semiconductors have a better energy resolution than scintillators. The semiconductor crystal band structures consist of two bands, the valence band and the conduction band. In pure semiconductors, the valence band is full of electrons whereas the conduction band is empty. The energy gap between

these bands is not large enough to prevent electrons from transferring from the valence band to the conduction band. So, if an electron has sufficient energy, larger than the energy gap, it will be excited and able to move from the valence band and across the energy gap to the conduction band. These electrons leave behind positive holes in the valence band. If the number of electrons is equal to the number of holes, the material is called an intrinsic semiconductor. Depending on the impurity, semiconductors are classified as two types: the p-type and the n-type. In n-type materials, the majority of charge carriers are electrons, whereas in the p-type the majority of charge carriers are holes. In order to create a sensitive volume in semiconductors detectors, a connection between the p-type and n-type must be made to make a p-n junction. This connection results in the migration of charge carriers. This migration creates a region empty of charge called the depletion region. This region can be made larger by applying a large reverse bias across the p-n junction. Radiation interacting in the depletion region then releases an electron-hole pair which goes to the two ends of the detector under the influence of the applied voltage.

3.6 High Purity Germanium Detectors

The thickness of the depletion region is defined by [31] :

$$d = \left(\frac{2\epsilon V}{eN}\right)^{\frac{1}{2}} \tag{3.6}$$

where: V is the reverse bias, N is the net impurity concentration, e is the electron charge, and ϵ is the dielectric constant. By using normal germanium, the largest depletion depth is 3 mm. This depth of depletion region is not sufficient in the case of gamma-ray detection because a gamma-ray is very penetrating. As can be seen in the previous equation, increasing the depth of the depletion region is possible by making a reduction in N. Thus, using hyper pure Germanium gives a larger depth of depletion region (1cm or more). High purity germanium (HPGe) must be cooled to liquid nitrogen temperature during operation to avoid thermal noise which arises because of the small band gap energy of 0.67 eV. HPGe detectors are constructed

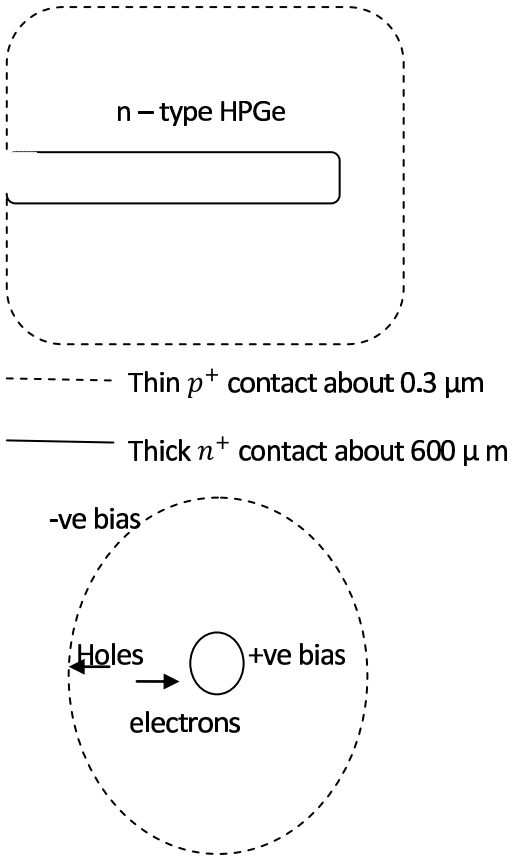

Figure 3.3: An illustration of the bulletised closed end coaxial configuration of the n-type HPGe detector.

in a bulletised coaxial configuration (see Figure 3.3), in order to create a detector with a large active volume. N-type detectors are usually used because they are less sensitive to neutron damage. This is because the signal is a result of the collection of electrons, which do not suffer from charge trapping as holes do. Also, at lower energy, the n-type is much more efficient than the p-type because of the thin window of n-type detectors.

3.7 Inorganic scintillators

Scintillation detectors are classified into two groups: organic scintillators and inorganic scintillators. Inorganic scintillators, made of high Z material, have a good light

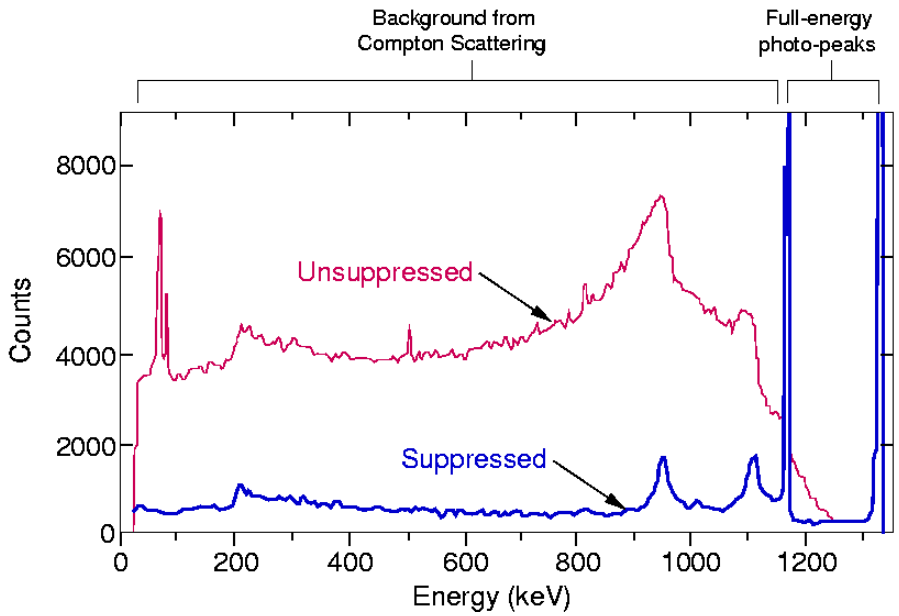

Figure 3.4: An illustration of the unsuppressed and suppressed spectra of a ^{60}Co source [36]

output, good linearity and high density. All of these properties make them efficient materials for gamma-ray detection. The main principle of their work is converting the absorbed gamma-ray into light, but this depends on the presence of an activator. Electrons are promoted from the valence band to the conduction band, due to the influence of ionising radiation, leaving behind holes in the valence band. These electrons and holes quickly drift to activator sites to recombine with the emission of optical photons. Without adding the activator the emitted photon following the absorption of radiation will lie in the invisible range. One of the good inorganic scintillators is the Bismuth Germanate (BGO) which has a high Z and high density. It does not require the addition of an impurity activator. It has a good light output and linearity. As a result of this characteristic, it is an attractive material for use in an anti-Compton escape suppression shield.

3.8 Escape Suppression

When γ-rays interact with the detector material, theoretically, the whole energy will be absorbed by the detectors material. This results in a spectrum corresponding to the full absorbed gamma-ray energy, but in fact the spectrum produced by a real detector has other features. These features are a result of the escape of some of the gamma-ray energy from the detectors material. This produces what is called a Compton background. This is a continuum of the background events which lie on an energy range from zero keV up to the Compton edge. The reduction in this continuum will improve the measurement of gamma-ray peaks. In order to reduce this unwanted effect, which reduces the quality of the spectrum, the germanium detectors are surrounded by high efficiency scintillators. One of the best choices of the scintillators is BGO due to its high density. BGO detectors detect the events scattered out of the HPGe then reject these events whose energy has not been deposited in full in the HPGe detector. In the GAMMASPHERE array, each HPGe detector is surrounded by six BGO crystals and a cylinder of BGO as a back-plug which covers the HPGe in order to suppress forward scattered photons. Each BGO scintillator is coupled to two photomultiplier tubes. The front surface of the BGO is covered with a heavy metal to block out the gamma-rays which go directly towards the BGO from the target, producing a false signal [32] (see Figure 3.4 and 3.5)

3.9 GAMMASPHERE

The GAMASPHERE array [33] is a most powerful spectrometer for Gamma-ray detection, which is located at the Argonne National Laboratory, USA. It is an array of escape suppressed n-type of HPGe detectors in a Hexagonal (honycomb) shape (see Figure 3.6). It consists of 101 detectors mounted in a 4π configuration around the target chamber. Each of these detectors is 71 mm in diameter and about 84 mm long. These detectors are arranged in angles around the target, with a forward-backward symmetry, with respect to the beam axis, as shown in table 3.1. The distance between

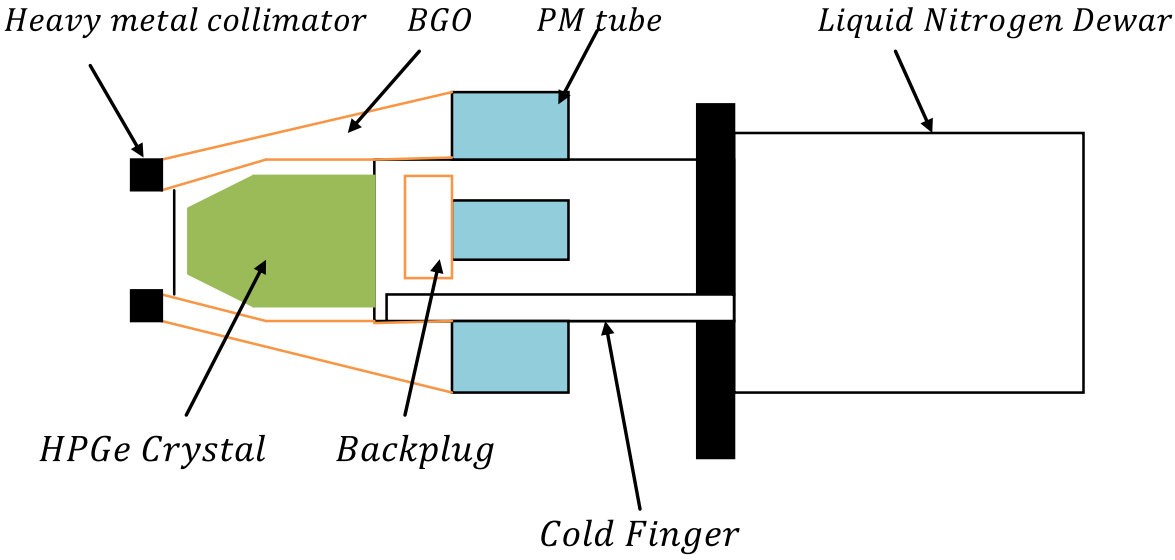

Figure 3.5: Schematic drawing of a GAMMASPHERE escape suppressed spectrometer.

the target and the the detector is about 248 mm. The good resolution, high efficiency and low background spectra of this array have led to the improvement of resolving power and the ability to identify weak cascades [34, 35].

3.10 Data Analysis

Such an array of detectors (i.e. GAMMASPHERE) makes it possible to detect more than one gamma ray simultaneously. By using this technique, the coincidence events can be arranged in matrices in order to construct and study the excitation pathway and level scheme. An example of these matrices is shown in Figure 3.7. In this matrix the coincident γ-rays are arranged in pairs for each event (for example event (1): a, b is arranged in two pairs as follow (a,b) and (b,a)). Then, recording these events in a symmetric matrix produces spectra of coincident γ-rays. By taking a single projection will show only γ-rays coincident with that energy. The coincidence data can be used to identify the decay paths by which a nucleus can lose energy and angular momentum. The level scheme can be constructed analytically by identifying

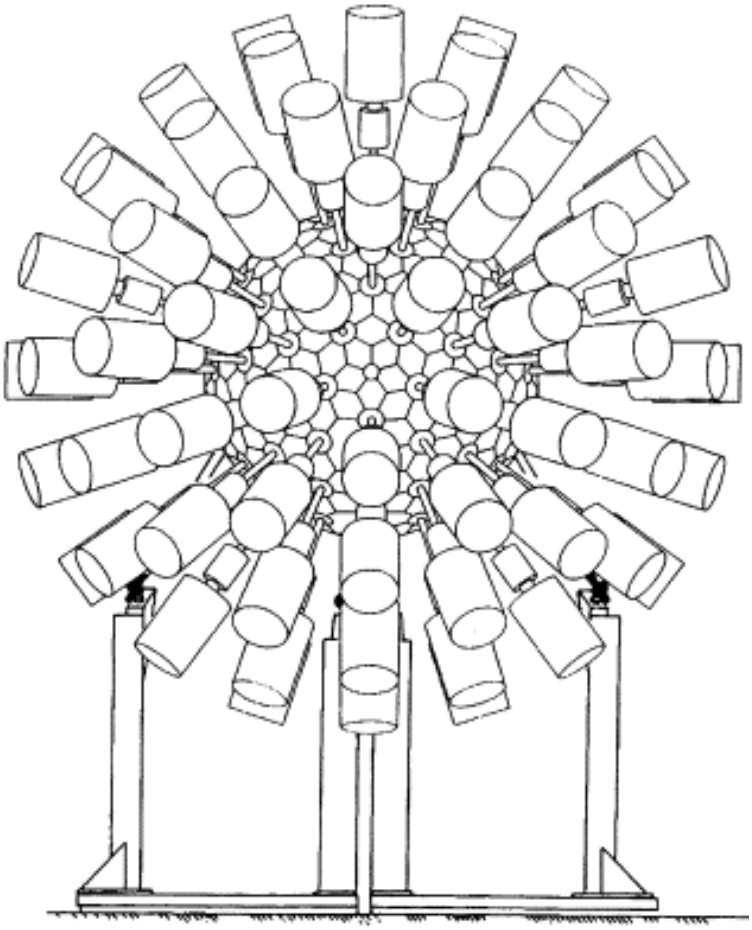

Figure 3.6: Schematic diagram of the GAMMASPHERE array showing the hexagonal (honeycomb) shape [35].

Angle	Number of Detectors
17.3^o	5
31.7^o	5
37.4^o	5
50.1^o	10
58.3^o	5
69.8^o	10
79.2^o	5
80.7^o	5
90^o	10
99^o	5
100.8^o	5
110.2^o	10
121.7^o	5
129.9^o	10
142.6^o	5
148.3^o	5
162.7^o	5

Table 3.1: This table shows the arrangement of the detectors with respect to beam axis

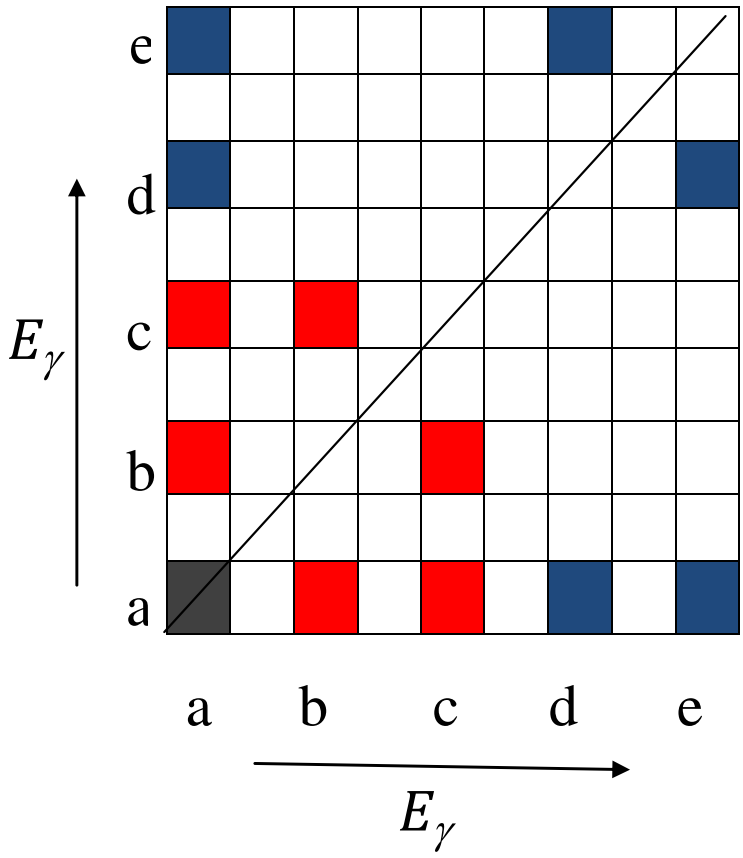

Figure 3.7: Schematic diagram showing an example of a symmetric matrix

the coincidence gamma rays. Gamma-ray emissions that lie on the same decay paths will be in coincidence whereas emission from a different path will not be as shown in figure 3.8. Techniques such as coincidence spectroscopy (γ-γ) matrices, (γ-γ-γ) cubes or even (γ-γ-γ-γ) hypercubes, have been used for energy and intensity measurement of the detected gamma-ray, to construct the level scheme and to study of the structure of the nucleus.

3.11 Angular Intensity Ratio

The experimental technique used to measure the angular intensity ratio is dependent on the alignment of the residual nuclei with their spin in a plane that is perpen-

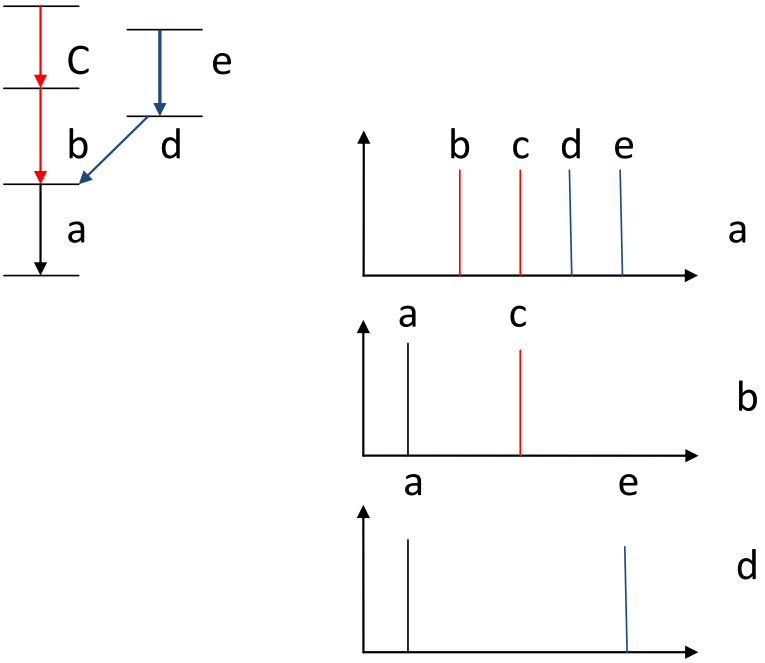

Figure 3.8: Schematic diagram showing the coincidences between gamma rays on the same decay path. The spectrum for transition (a) shows all other transitions as they all feed the state above it. whereas the spectrum for b (d) does not show transitions d (b) or e (c), respectively, since they are not emitted in the same decay path.

dicular to the beam axis through the heavy-ion fusion-evaporation reaction [37, 38]. This technique provides information about the multipolarity of the emitted gamma-rays. In this work, the MIDAS software has been used to sort unfolded data into γ-γ matrices, by setting lists of gates on coincidence transitions that produce one dimensional spectra for the coincidence transitions at different detector ring angles of the Gammasphere array relative to the beam direction. The angular intensity ratio of a specific gamma-ray has been identified from the intensity measurements (I_γ), which were detected by detectors positioned near (35°) and (145°) angles, and near (90°), perpendicular to the beam axis. Thus, the angular intensity ratio can be defined as:

$$R = \frac{I_\gamma[\theta \sim 145°(35°)]}{I_\gamma[\theta \sim 90°)]} \tag{3.7}$$

where I_γ is the intensity of the gamma-ray. The approximate extracted values of the angular Intensity measurements from this work are approximately 0.5 for pure stretched dipole transitions and 1.0 for stretched quadrupole transitions. These values were measured from some known transitions of previous work [48].

Chapter 4

^{131}Ce Results

4.1 Introduction

The odd-N nuclei in the $A \sim 130$ region have a wealth of nuclear structure information. One of the interesting features is related to the negative-parity yrast bands, built on $\nu h_{11/2}$ orbitals from the upper midshell, which exhibit a large signature splitting. This signature splitting initially increases with spin, then, after the alignment of a proton pair it decreases to almost zero. In these bands it is believed that the $\nu h_{11/2}$ orbitals drive the nuclear shape to triaxial with $\gamma < 0^{\circ}$ [9, 39]. Thus, these nuclei exhibit triaxial shape at low spin. Whereas the proton Fermi surface lies near the $\pi h_{11/2}$ orbitals which favour a prolate shape [40, 41]. Hence, these nuclei show triaxiality at low spin and near axiality at high spin. This deformation is well described by the triaxiality parameter γ, which has a greater influence on the crossing frequency than the quadruple deformation β [42]. In this mass region at low spin odd-proton nuclei tend to be axially symmetric where as odd-neutron nuclei are expected to be triaxial. The nucleus ^{131}Ce has been studied using the reaction ^{100}Mo(^{36}S,5nγ) at 165 MeV. The gamma ray coincidence data produced by this reaction at Argonne National Laboratory , USA, were recorded with GAMMASPHERE. A quadruple coincidence analysis of this data established two new band structures and extended some of the known bands to higher spin. Signature splitting was observed at low

spin about 130 keV indicates to a significant triaxial deformation ($\gamma \sim -26°$). The suggested configuration for these bands (eEF, fEF) based on comparing their properties with Wood-Saxon cranking calculations and theoretical B(M1)/B(E2) ratios of reduced transition probabilities. The angular intensity-ratio measurements have been performed to gain information on the multipolarities of transitions in this nucleus.

4.2 Experimental Details

The high-spin states of ^{131}Ce were populated using the ^{100}Mo(^{36}S,5nγ) fusion evaporation reaction carried out at Argonne National laboratory, USA. The beam of ^{36}S was produced by the ATLAS accelerator to an energy of 165 MeV with a beam current of 5 pnA. This beam bombarded two enriched self-supporting foils of ^{100}Mo each of which has a thickness of 600 μg/cm^2. The GAMMASPHERE array consisting of 101 Compton-suppressed Hyper-Pure Germanium Detectors [34, 43] was used to record gamma-ray events. The total run time for this experiment was 18×8 hour shifts. A total of 3×10^9 events of fold $k \geq 7$ were recorded. These data were unfolded off-line into quadruple coincidence events and replayed into a 4-dimensional hypercube. The analysis was carried out using 4DG8R software [44, 45].

4.3 ^{131}Ce Results

The deduced level scheme for ^{131}Ce from the present work is shown in figure 4.1. The ordering of transitions within the proposed level scheme is based on gamma-ray coincidences and their relative intensities. The gamma-ray multipolarities were extracted using the angular intensity-ratio measurements. Gamma-ray energies, relative intensities, angular intensity-ratio measurements, spins and parities are listed in Tables 4.1, 4.2, 4.3, 4.4, 4.5, 4.6 and 4.7. The relative intensities were normalised to the intensity of the 508 keV $15/2^- \rightarrow 11/2^-$ transition. The angular intensity-ratio values were approximately 0.5 for pure stretched dipole transition and 1.0 for

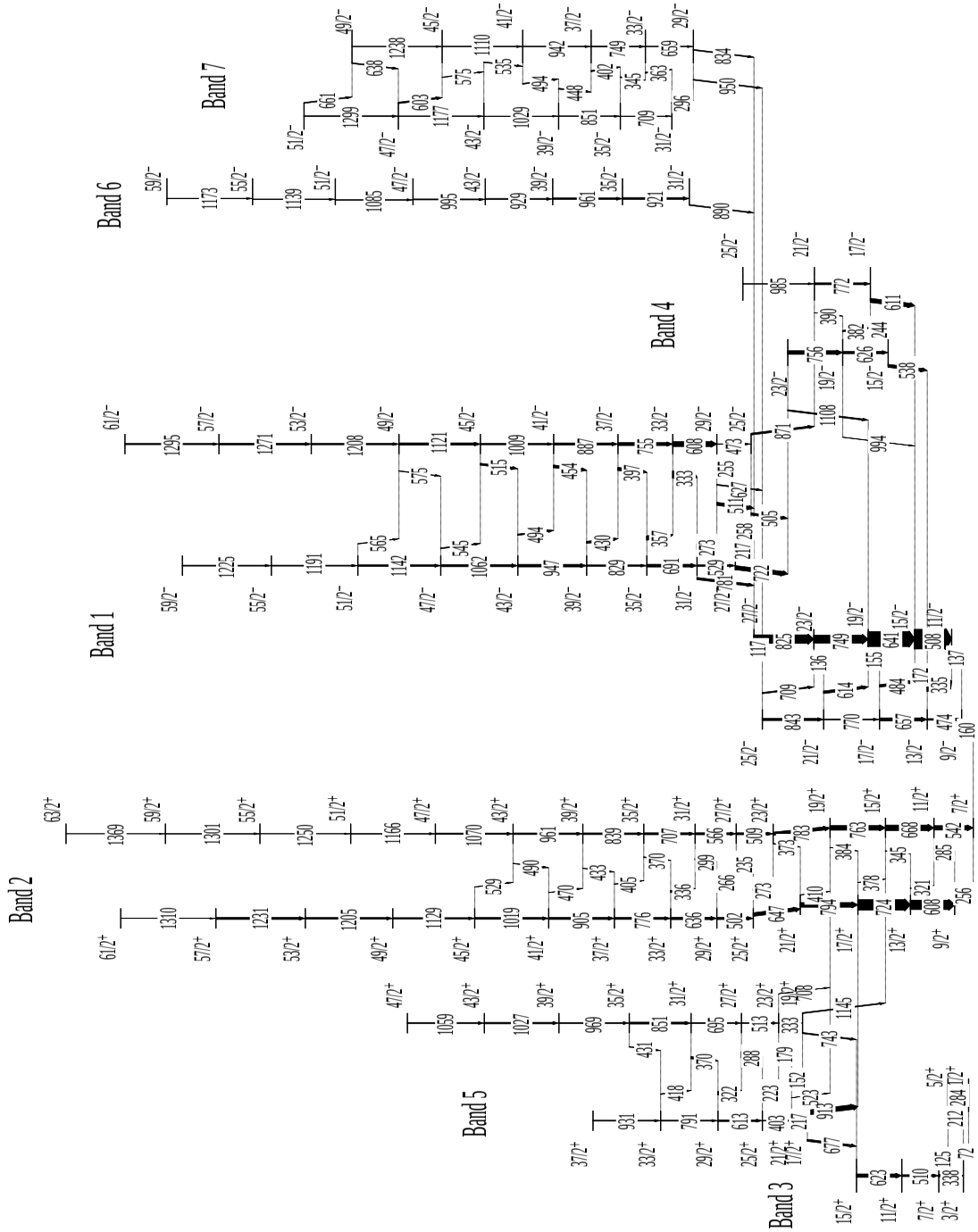

Figure 4.1: The level scheme deduced for ^{131}Ce from this work. The width of the arrows is proportional to the relative intensity and energies are labelled in keV.

stretched quadrapole transitions (E2). The experimental results will be discussed in two sections, one for the negative parity bands and one for the positive parity bands.

4.3.1 The Negative-parity bands

Band 1

This negative-parity structure was identified in Ref. [47] up to spin $49/2^-$. The band is extended in this work up to spin $61/2^-$ by a further six new E2 transitions 1142, 1191, 1208, 1225, 1271 and 1295 keV and three M1/E2 transitions 545, 575 and 565 keV. This band feeds band 4 through the newly found transitions (871 keV) E2 and (505 keV) M1/E2 transitions. Figures 4.2, 4.3 and 4.4 show the spectra of the extended left and right sides of band 1 together with their interlinking M1/E2 transitions, respectively, and Figure 4.5 shows the double gated spectrum showing the newly found 505 keV transition linking band 1 to band 4. Gamma-ray energies, relative intensities, angular intensity-ratio measurements, spins and parities for this band are listed in Tables 4.1 and 4.2.

Band 4

Some of the γ-transitions in this negative structure were observed in Ref [47]. In this work this structure is expanded to build a coupled band. All M1/E2 transitions are newly found in this work. The E2 transitions observed in this work are 772 and 985 keV. The band feeds band 1 through a new dipole transition (611 keV). Figure 4.6 shows the spectrum of this band and the new transitions observed in the present work. Gamma-ray energies, relative intensities, angular intensity-ratio measurements, spins and parities for this band are listed in Table 4.4.

Band 6

This band which is labelled in Figure 4.1 as band 6 was established up to $I^\pi = 31/2^-$ by Gizon et al. [47]. It was then extended up to $I^\pi = 35/2^-$ by Nolan et al. [48]

and further extended up to $I^{\pi} = 39/2^{-}$ in Ref. [49] . In this work higher excited states up to $I^{\pi} = (59/2^{-})$ are observed. Figure 4.7 shows the triple-gated spectrum showing the new extent of band 6. Gamma-ray energies, relative intensities, angular intensity-ratio measurements, spins and parities for this band are listed in Table 4.3.

Band 7

The strongly coupled structure, labelled band 7 in Fig. 4.1, is newly found in this work and consists of 10 E2 transitions and 11 M1/E2 transitions. It depopulates to band 1 by a $29/2^{-} \rightarrow 25/2^{-}$ E2 transition (950 keV) and by a $29/2^{-} \rightarrow 27/2^{-}$ dipole M1/E2 transition (834 keV). The band head is determined to be $29/2^{-}$ based on the angular intensity measurements. Figure 4.8 shows the spectrum of band 7. Gamma-ray energies, relative intensities, spins and parities for this band are listed in Table 4.3.

4.3.2 The positive-parity bands

Band 2

This positive parity structure is labelled band 2 in Figure 4.1. The band was established in Ref. [47] up to spin $23/2^{+}$ and it has been extended up to spin $35/2^{+}$ in Ref [48]. It was also observed by Gizon et al. [49]. It was then extended up to spin $51/2^{+}$ by Palacz et al. [50] but in this work the last transitions, 1155 keV, was amended to 1166 keV. This structure is extended in the present work up to spin $63/2^{+}$ by seven new transitions. Figures 4.9 and 4.10 show the spectra of the extended left and right sides of band 2, respectively. Gamma-ray energies, relative intensities, angular intensity-ratio measurements, spins and parities are listed in Tables 4.5 and 4.6.

Band 3

This band was observed in Ref [48]. It is linked to the $\Delta I = 1$ band, band 5, by two transitions of 677 and 743 keV. It is confirmed in this work. Figure 4.11 shows the

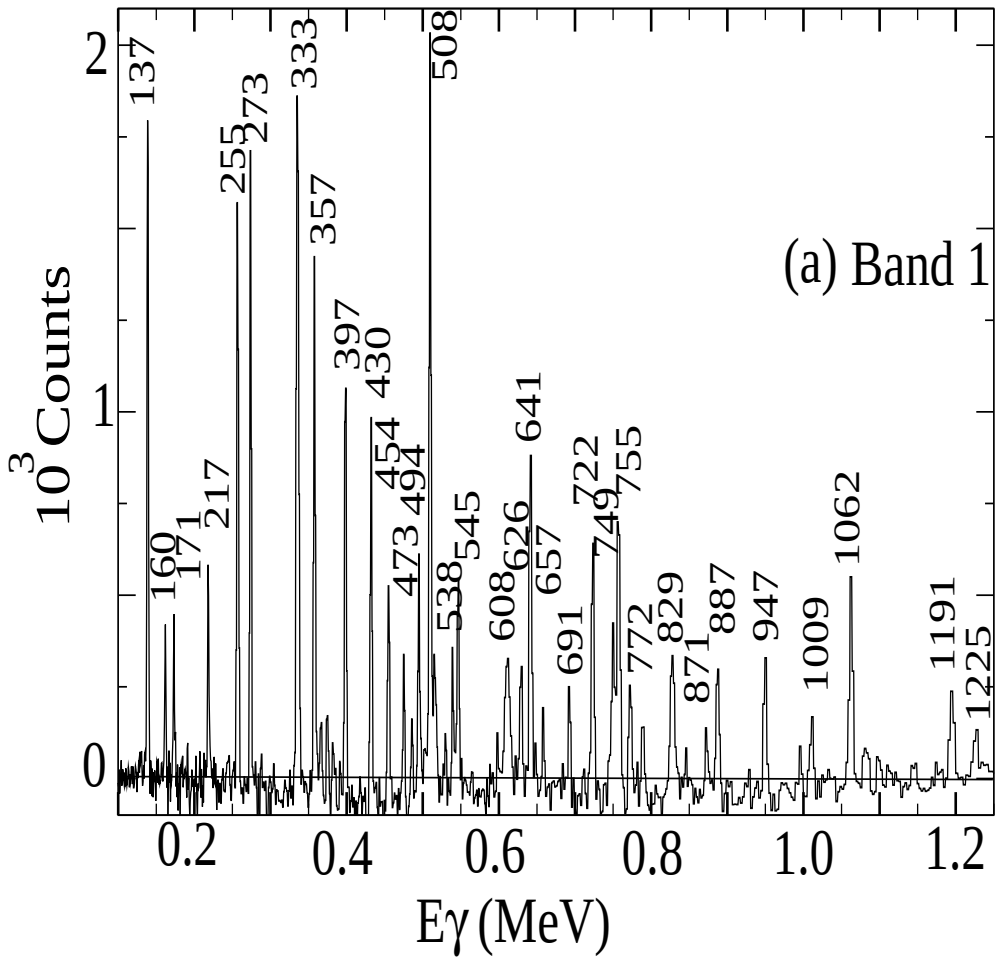

Figure 4.2: A spectrum showing the new extension of the left side of band 1 produced from a sum of triple gates (x, y = list of gates on M1/E2 transitions up to 515 keV, z = 1142 keV).

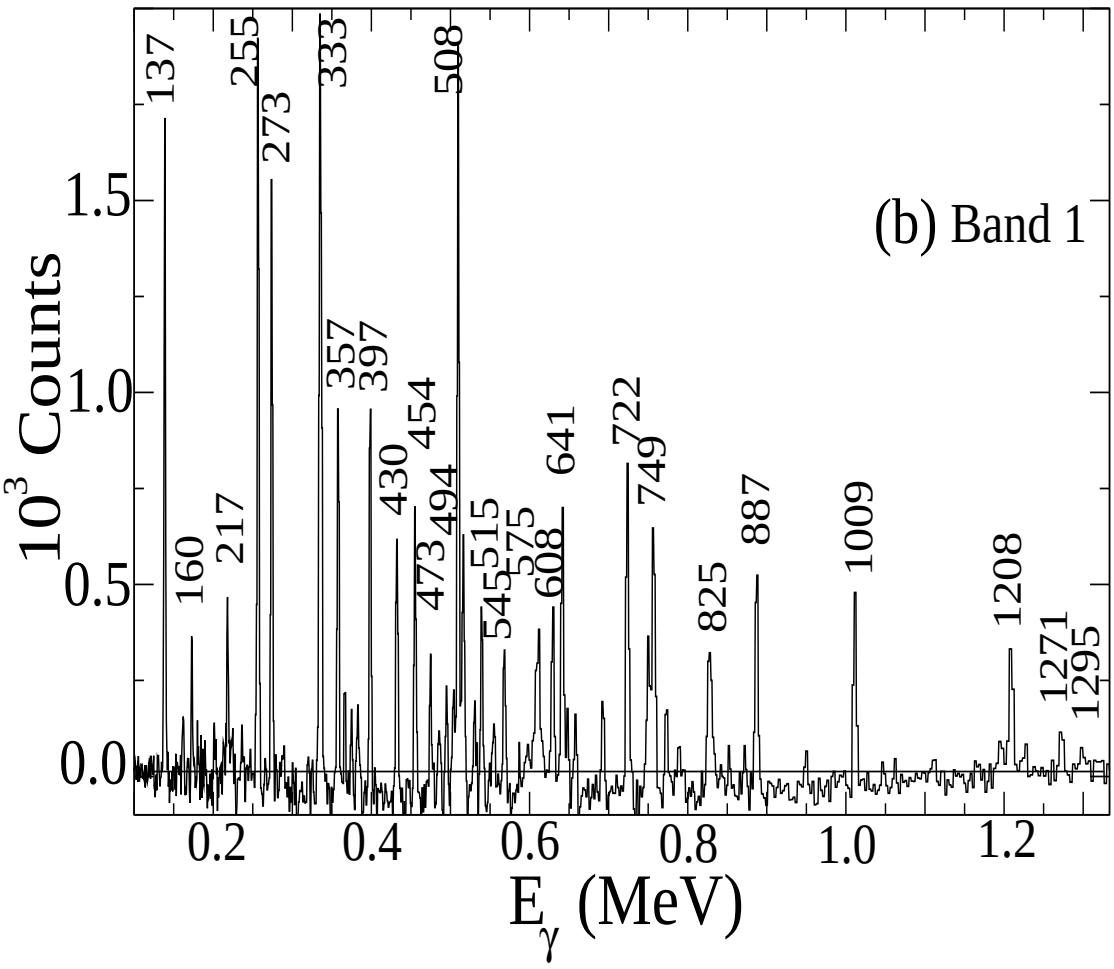

Figure 4.3: A spectrum showing the new extension of the right side of band 1 produced from a sum of triple gates (x, y = list of gates on M1/E2 up to 515 keV, z = 1121 keV).

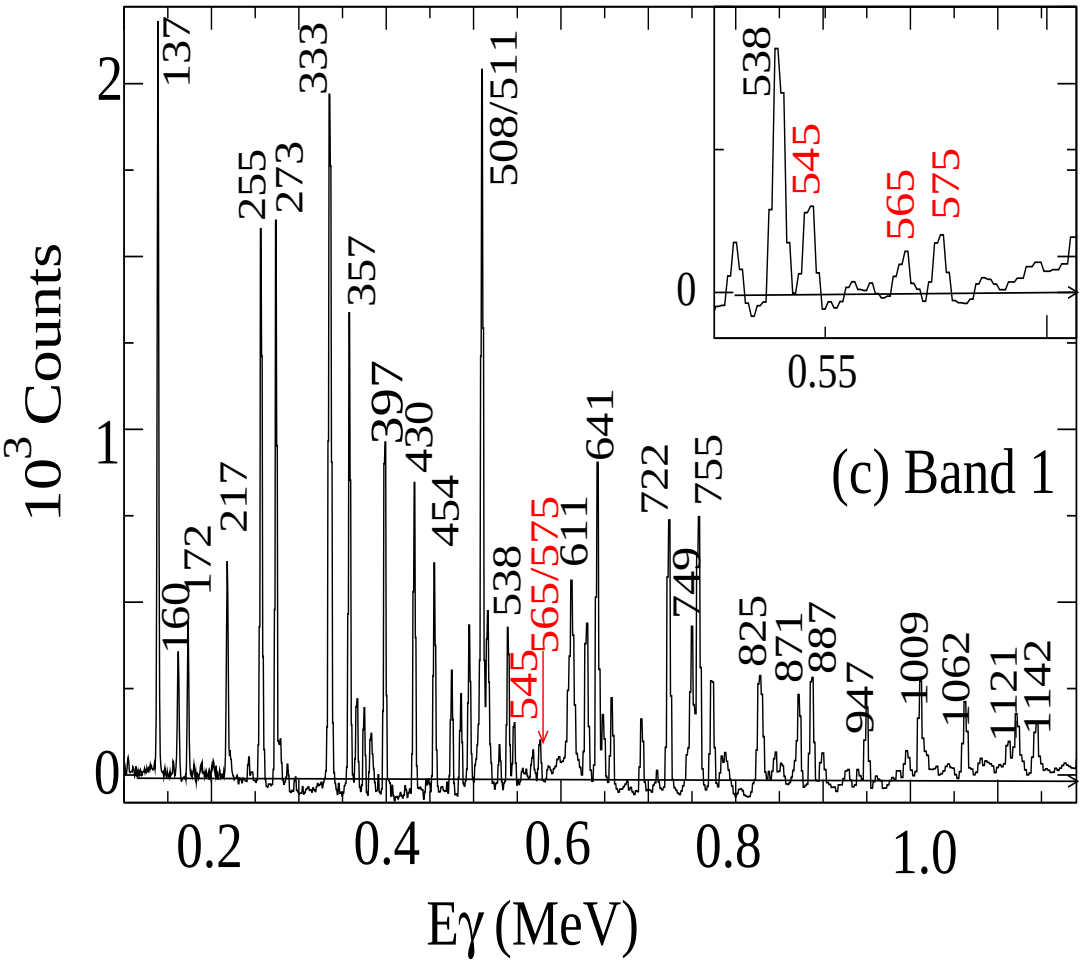

Figure 4.4: A spectrum produced from a sum of triple gates (x, y, z = list of gates on M1/E2 up to 515 keV) showing the extension of the M1 transitions (red) of band 1.

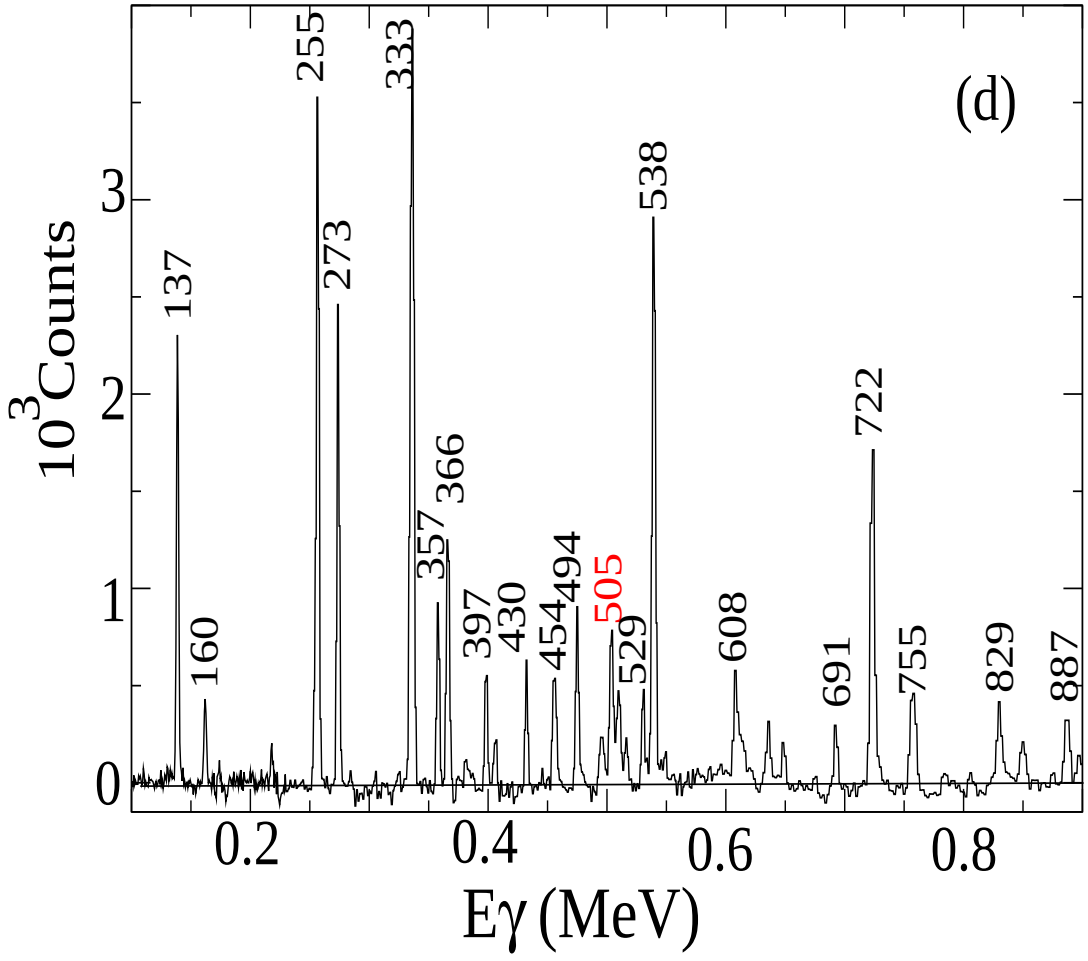

Figure 4.5: The double gated spectrum (x = 756 keV, y = 626 keV) showing the newly found 505 transition (red) link band 1 to band 4.

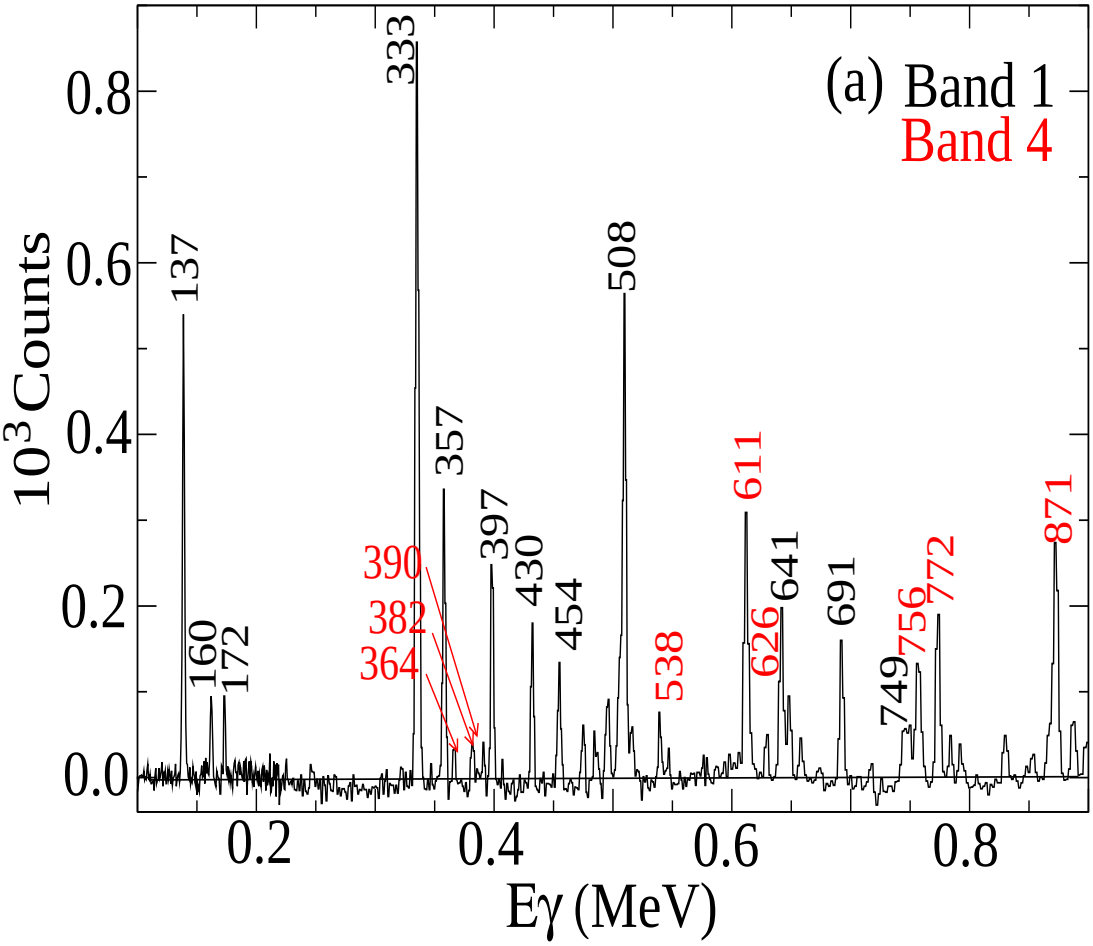

Figure 4.6: The triple gated spectrum (x = 217 keV, y = 255 keV, z = 273 keV) showing band 4 (red) and band 1 (black).

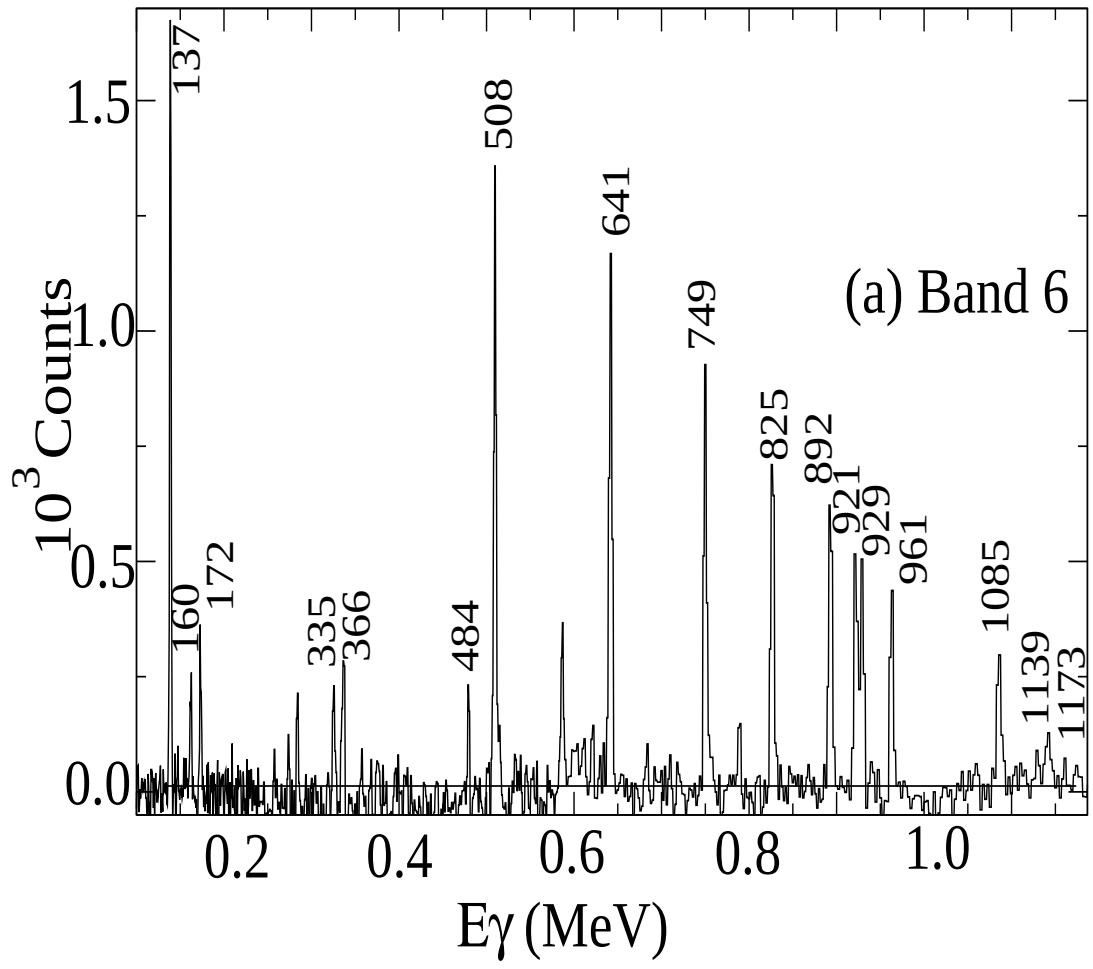

Figure 4.7: A spectrum produced from a sum of triple gates (x, y = list of gates on E2 up to 929 keV, z = 995 keV) showing the new extension in band 6.

double-gated spectrum for band 3. Gamma-ray energies, relative intensities, angular intensity-ratio measurements, spins and parities for this band are listed in Table 4.4.

Band 5

No new transitions are observed in this band from the present work. This positive-parity structure was observed up to spin $49/2^+$ in Ref [50]. The band head of this band was confirmed by Gizon et al. [49]. It is linked to band 2 by 708, 913, and 1145 keV transitions and to band 3 by 677 and 743 keV transitions. Gamma-ray energies, relative intensities, angular intensity-ratio measurements, spins and parities for this band are listed in Table 4.7.

E_γ (keV)	I_γ	R	Assignment
Band 1 quadrupoles (E2)			
507.9	100	0.94±0.02	$15/2^- \rightarrow 11/2^-$
641.2	75.5±3.1	1.06±0.04	$19/2^- \rightarrow 15/2^-$
749.3	42.3±2.1	1.30±0.09	$23/2^- \rightarrow 19/2^-$
825.4	38.2±1.8	0.97±0.06	$27/2^- \rightarrow 23/2^-$
473.8	4.0±0.3	0.91±0.09	$29/2^- \rightarrow 25/2^-$
607.5	26.1±1.5	1.17±0.03	$33/2^- \rightarrow 29/2^-$
755.4	15.7±0.9	1.03±0.06	$37/2^- \rightarrow 33/2^-$
887.3	11.7±0.6	1.16±0.05	$41/2^- \rightarrow 37/2^-$
1008.8	8.0±0.4	0.94±0.05	$45/2^- \rightarrow 41/2^-$
1120.7	7.1±0.5	0.86±0.08	$49/2^- \rightarrow 45/2^-$
1208	7.6±0.8	1.12±0.09	$53/2^- \rightarrow 49/2^-$
691.4	34.2±0.9	1.15±0.08	$35/2^- \rightarrow 31/2^-$
829.3	21.1±1.3	0.95±0.05	$39/2^- \rightarrow 35/2^-$
947.4	11.2±1.1	1.03±0.05	$43/2^- \rightarrow 39/2^-$
1062	9.5±0.9	0.88±0.09	$47/2^- \rightarrow 43/2^-$
1142.4	8.6±0.8	1.12±0.09	$51/2^- \rightarrow 47/2^-$
780.6	12.1±0.6	1.18±0.08	$31/2^- \rightarrow 27/2^-$

Table 4.1: Gamma-ray energies, relative intensities, angular intensity-ratio measurements, spins and parities for the transitions assigned to band 1 where the intensities are given relative to the 508 keV transition of band 1.

E_γ (keV)	I_γ	R	Assignment
Band 1 dipoles (M1/E2)			
137.4	68.3±3.2	0.50±0.04	$11/2^- \rightarrow 9/2^-$
171.8	26.0±1.6	0.50±0.04	$15/2^- \rightarrow 13/2^-$
154.8	10.2±0.6	0.45±0.06	$19/2^- \rightarrow 17/2^-$
335.4	30.1±2.9	0.61±0.05	$13/2^- \rightarrow 11/2^-$
483.8	6.7±0.7	0.42±0.06	$17/2^- \rightarrow 15/2^-$
216.7	8.2±0.6	0.57±0.09	$27/2^- \rightarrow 25/2^-$
255.4	36.0±1.8	0.65±0.04	$29/2^- \rightarrow 27/2^-$
272.7	28.3±1.2	0.52±0.05	$31/2^- \rightarrow 29/2^-$
333.1	25.0±1.3	0.54±0.07	$33/2^- \rightarrow 31/2^-$
356.7	21.0±1.1	0.56±0.06	$35/2^- \rightarrow 33/2^-$
396.7	14.7±0.8	0.42±0.07	$37/2^- \rightarrow 35/2^-$
430.4	10.7±0.4	0.52±0.07	$39/2^- \rightarrow 37/2^-$
454.2	10.2±0.3	0.57±0.09	$41/2^- \rightarrow 39/2^-$
494.1	6.6±0.6	0.54±0.08	$43/2^- \rightarrow 41/2^-$
515.3	6.1±0.5	0.71±0.07	$45/2^- \rightarrow 43/2^-$
544.9	6.0±0.6	0.49±0.09	$47/2^- \rightarrow 45/2^-$
504.9	9.2±0.7	0.61±0.08	$25/2^- \rightarrow 23/2^-$

Table 4.2: Gamma-ray energies, relative intensities, angular intensity-ratio measurements, spins and parities for the transitions assigned to band 1 where the intensities are given relative to the 508 keV transition of band 1.

E_γ (keV)	I_γ	R	Assignment
Band 6 quadrupoles (E2)			
890.8	20.0±1.1	1.12±0.06	$31/2^- \rightarrow 27/2^-$
920.8	12.2±0.8	0.94±0.08	$35/2^- \rightarrow 31/2^-$
960.8	8.5±0.7	1.19±0.07	$39/2^- \rightarrow 35/2^-$
928.7	7.0±0.5	1.10±0.14	$43/2^- \rightarrow 39/2^-$
995.4	5.1±0.4	0.95±0.12	$47/2^- \rightarrow 43/2^-$
Band 7 quadrupoles (E2)			
950.3	24.3±1.4	1.01±0.03	$29/2^- \rightarrow 25/2^-$
1110.2	6.9±0.7	0.76±0.09	$45/2^- \rightarrow 41/2^-$
709.1	16.3±0.9	1.01±0.12	$35/2^- \rightarrow 31/2^-$
749.2	6.0±0.5	0.81±0.08	$37/2^- \rightarrow 33/2^-$
1176.7	3.1±0.2	1.09±0.09	$47/2^- \rightarrow 43/2^-$
850.8	4.0±0.2	0.92±0.16	$39/2^- \rightarrow 35/2^-$
Band 7 dipoles (M1/E2)			
295.6	32.1±1.3	0.5±0.04	$33/2^- \rightarrow 31/2^-$
363.4	26.4±1.1	0.56±0.08	$35/2^- \rightarrow 33/2^-$
346	23.0±1.2	0.48±0.09	$37/2^- \rightarrow 35/2^-$
403.2	12.0±0.6	0.51±0.04	$39/2^- \rightarrow 37/2^-$
447.7	10.4±0.9	0.44±0.06	$41/2^- \rightarrow 39/2^-$
494.2	10.1±0.8	0.42±0.07	$43/2^- \rightarrow 41/2^-$
535.3	5.6±0.3	0.53±0.11	$45/2^+ \rightarrow 43/2^-$
575.9	39.0±1.5	0.65±0.05	$45/2^- \rightarrow 43/2^-$
601.8	5.3±0.3	0.46±0.12	$49/2^- \rightarrow 47/2^-$
834.2	25.4±1.4	0.61±0.05	$29/2^- \rightarrow 27/2^-$

Table 4.3: Gamma-ray energies, relative intensities, angular intensity-ratio measurements, spins and parities for the transitions assigned to bands 6 and 7 where the intensities are given relative to the 508 keV transition of band 1.

E_γ (keV)	I_γ	R	Assignment
Band 3 quadrupoles (E2)			
338.1	11.3±0.4	0.94± 0.04	$7/2^+ \rightarrow 3/2^+$
509.9	9.9±0.9	0.72±0.06	$11/2^+ \rightarrow 7/2^+$
623.4	9.4±0.8	1.14±0.07	$15/2^+ \rightarrow 11/2^+$
743.3	6.2±0.5	1.01±0.08	$19/2^+ \rightarrow 15/2^+$
Band 4 quadrupoles (E2)			
625.8	31.8±1.4	0.84±0.05	$19/2^- \rightarrow 15/2^-$
755.6	38.5±1.8	1.17±0.06	$23/2^- \rightarrow 19/2^-$
771.5	39.9±1.3	0.95±0.03	$21/2^- \rightarrow 17/2^-$
984.8	12.1±0.5	1.1±0.07	$25/2^- \rightarrow 21/2^-$
871.2	16.2±0.7	0.98±0.03	$19/2^- \rightarrow 15/2^-$
994.3	20.3±0.8	1.12±0.04	$19/2^- \rightarrow 15/2^-$
1108	10.3±0.4	0.9±0.06	$23/2^- \rightarrow 19/2^-$
Band 4 dipoles (M1/E2)			
243.7	5.1±0.3	0.51±0.06	$17/2^- \rightarrow 15/2^-$
382.1	3.2±0.2	0.61±0.03	$19/2^- \rightarrow 17/2^-$
390.1	4.6±0.3	0.57±0.04	$21/2^- \rightarrow 19/2^-$
363.8	13.8±0.6	0.67±0.03	$23/2^- \rightarrow 21/2^-$
611.1	25.2±1.1	0.56±0.02	$17/2^- \rightarrow 15/2^-$
538.3	19.3±0.9	0.55±0.03	$15/2^- \rightarrow 13/2^-$

Table 4.4: Gamma-ray energies, relative intensities, angular intensity-ratio measurements, spins and parities for the transitions assigned to bands 3 and 4 where the intensities are given relative to the 508 keV transition of band 1.

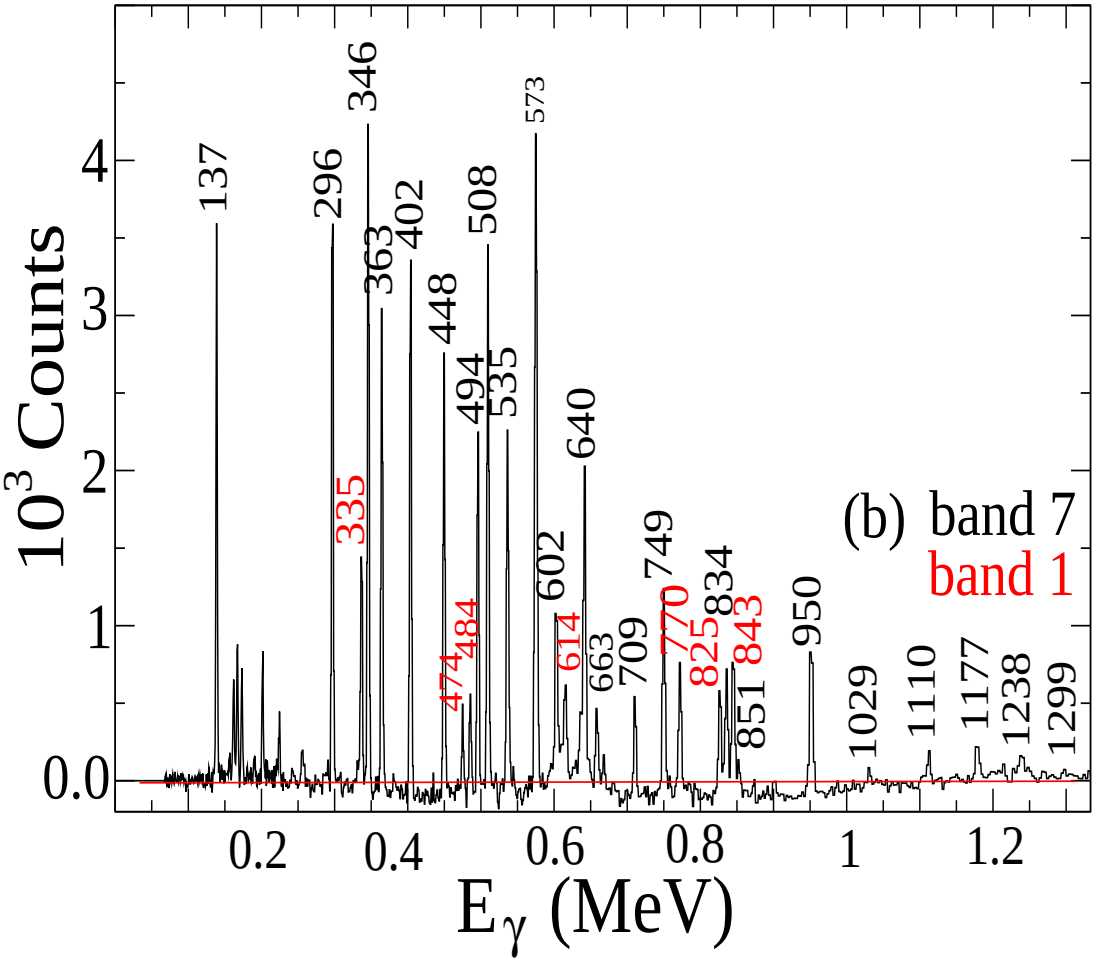

Figure 4.8: A spectrum of band 7 produced from a sum of triple gates (x, y, z = list of gates on M1/E2 transitions).

E_γ (keV)	I_γ	R	Assignment
Band 2 quadrupoles (E2)			
542.2	22.9±1.3	1.04±0.03	$11/2^+ \rightarrow 7/2^+$
667.6	29.1±1.4	1.09±0.02	$15/2^+ \rightarrow 11/2^+$
763.4	24.4±1.2	1.21±0.03	$19/2^+ \rightarrow 15/2^+$
783.4	16.7±0.6	1.16±0.04	$23/2^+ \rightarrow 19/2^+$
509.1	10.5±0.4	0.85±0.06	$27/2^+ \rightarrow 23/2^+$
566.2	10.0±0.5	1.01±0.07	$31/2^+ \rightarrow 27/2^+$
707.4	10.1±0.3	1.06±0.05	$35/2^+ \rightarrow 31/2^+$
839.4	8.9±0.8	1.1±0.09	$39/2^+ \rightarrow 35/2^+$
960.8	8.5±0.7	1.16±0.03	$43/2^+ \rightarrow 39/2^+$
1069.9	7.5±0.6	1.04±0.12	$47/2^+ \rightarrow 43/2^+$
1165.8	4.4±0.3	1.09±0.19	$51/2^+ \rightarrow 47/2^+$
607.7	48.5±2.3	1.17±0.02	$13/2^+ \rightarrow 9/2^+$
723.7	45.2±2.1	1.16±0.01	$17/2^+ \rightarrow 13/2^+$
793.6	23.9±1.2	0.90±0.03	$21/2^+ \rightarrow 17/2^+$
647.4	17.8±0.7	1.22±0.04	$25/2^+ \rightarrow 21/2^+$
502.1	11.2±0.6	1.14±0.08	$29/2^+ \rightarrow 25/2^+$
635.7	12.0±0.4	1.18±0.07	$33/2^+ \rightarrow 29/2^+$
775.6	10.7±0.6	1.07±0.05	$37/2^+ \rightarrow 33/2^+$
904.6	11.2±0.5	1.09±0.05	$41/2^+ \rightarrow 37/2^+$
1019.3	10.1±0.4	1.23±0.03	$45/2^+ \rightarrow 41/2^+$
1128.6	7.6±0.6	0.98±0.03	$49/2^+ \rightarrow 45/2^+$
1204.7	9.1±0.5	1.06±0.16	$53/2^+ \rightarrow 49/2^+$
1231.3	9.2±0.4	0.88±0.14	$57/2^+ \rightarrow 53/2^+$

Table 4.5: Gamma-ray energies, relative intensities, angular intensity-ratio measurements, spins and parities for the transitions assigned to band 2 where the intensities are given relative to the 508 keV transition of band 1.

E_γ (keV)	I_γ	R	Assignment
Band 2 dipoles (M1/E2)			
255.8	5.1±0.4	0.56±0.01	$9/2^+ \rightarrow 7/2^+$
285.1	39.3±1.7	0.61±0.02	$11/2^+ \rightarrow 9/2^+$
344.9	28.1±1.2	0.52±0.07	$13/2^+ \rightarrow 11/2^+$
410.1	22.1±1.3	0.59±0.16	$15/2^+ \rightarrow 13/2^+$
372.9	22.0±0.9	0.61±0.02	$23/2^+ \rightarrow 21/2^+$
235.3	20.3±0.9	0.59±0.06	$27/2^+ \rightarrow 25/2^+$
266.1	20.0±1.1	0.47±0.07	$29/2^+ \rightarrow 27/2^+$
299.4	25.4±1.5	0.55±0.09	$31/2^+ \rightarrow 29/2^+$
336.4	20.2±0.8	0.49±0.01	$33/2^+ \rightarrow 31/2^+$
370.1	14.3±0.6	0.50±0.04	$35/2^+ \rightarrow 33/2^+$
404.8	6.4±0.5	0.51±0.05	$37/2^+ \rightarrow 35/2^+$
432.9	7.1±0.4	0.47±0.07	$39/2^+ \rightarrow 37/2^+$
469.9	5.6±0.6	0.62±0.19	$41/2^+ \rightarrow 39/2^+$
490.3	4.2±0.3	0.61±0.21	$43/2^+ \rightarrow 41/2^+$

Table 4.6: Gamma-ray energies, relative intensities, angular intensity-ratio measurements, spins and parities for the transitions assigned to band 2 where the intensities are given relative to the 508 keV transition of band 1.

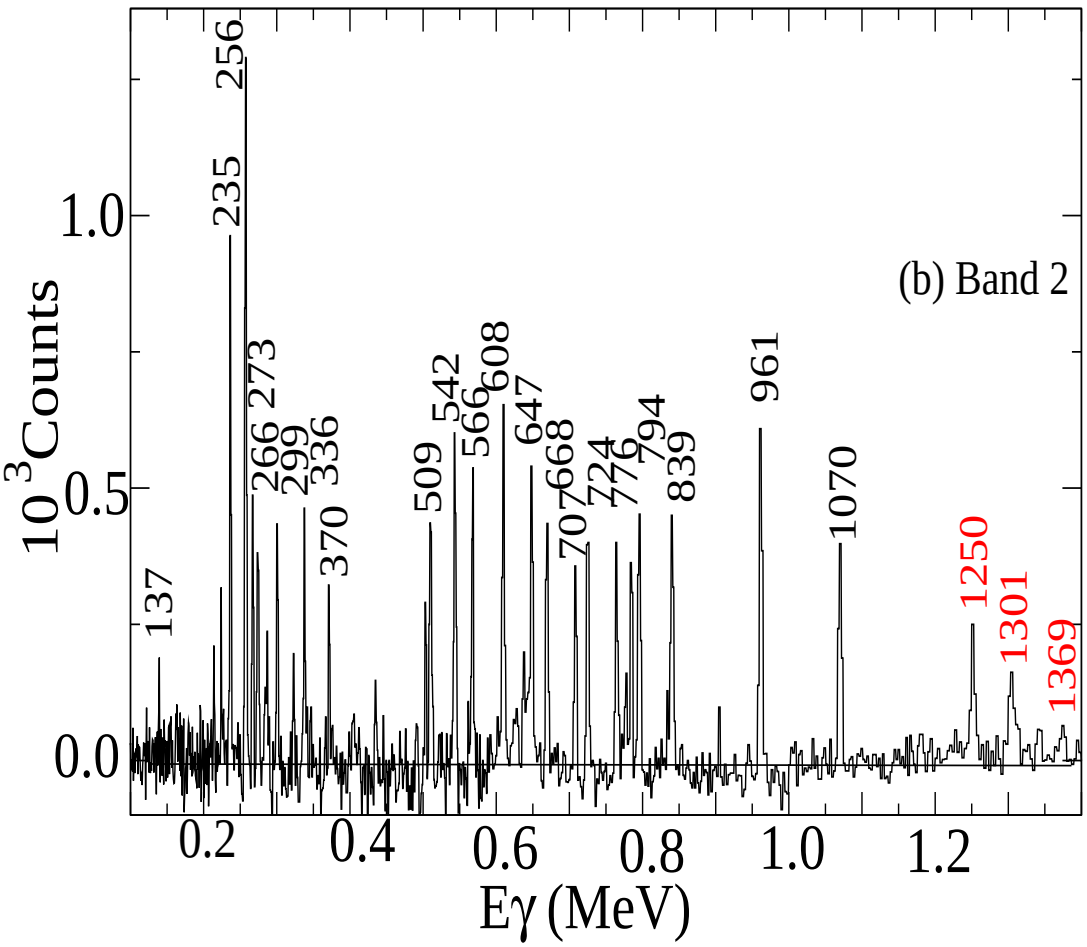

Figure 4.9: A spectrum of the right side of band 2 produced from a sum of triple gates (x = list of gates on E2 transitions up to 1070 keV, y = list of gate on M1 up to 490 keV, z = 1166 keV).

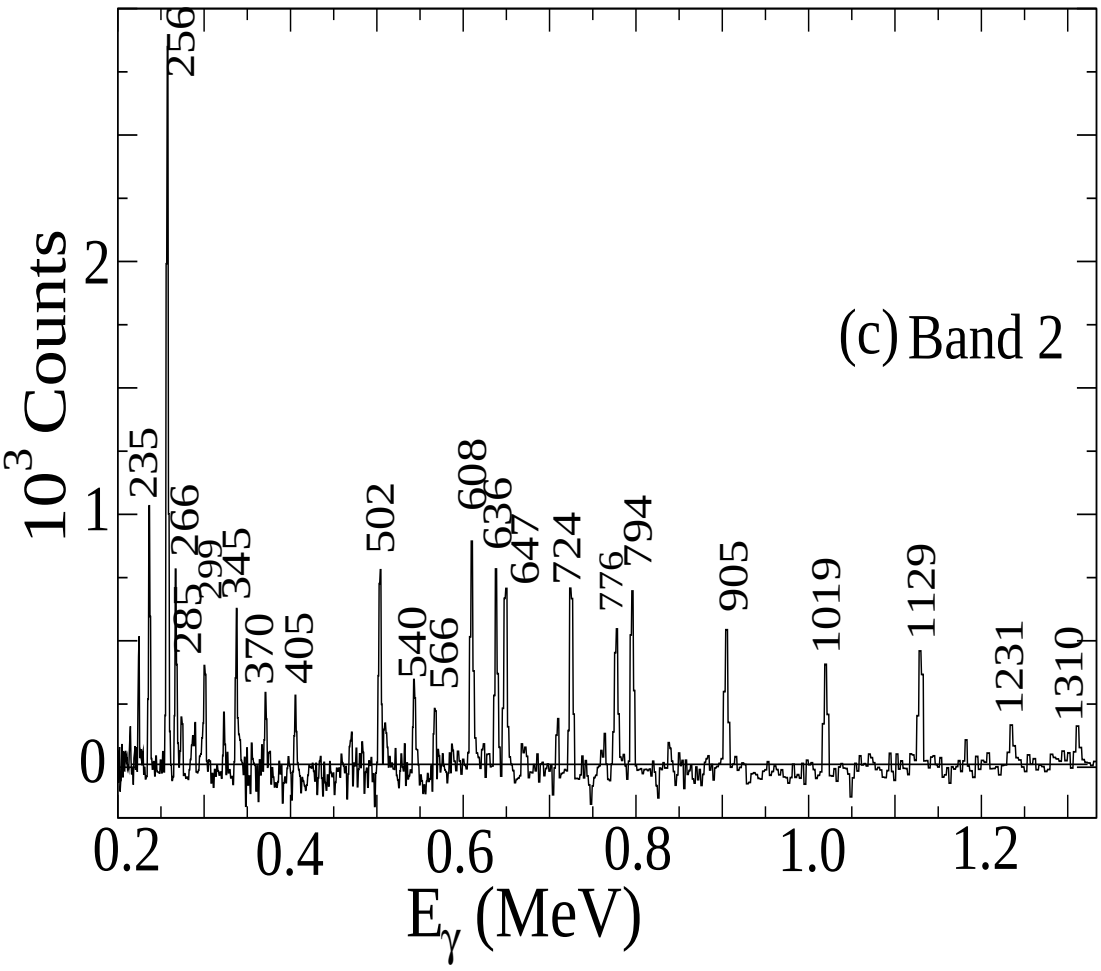

Figure 4.10: A spectrum of the lift side of band 2 produced from a sum of triple gates (x = list of gates on E2 transitions up to 1129 keV, y = list of gate on M1/E2 up to 529 keV, z = 1205 keV).

E_γ (keV)	I_γ	R	Assignment
Band 5 quadrupoles (E2)			
333.1	15.3±0.8	0.99±0.02	$19/2^+ \rightarrow 15/2^+$
512.7	16.4±0.7	1.21±0.08	$23/2^+ \rightarrow 19/2^+$
695.1	10.1±0.6	1.06±0.07	$27/2^+ \rightarrow 23/2^+$
851.3	10.0±0.4	1.23±0.14	$31/2^+ \rightarrow 27/2^+$
968.6	6.9±0.5	0.92±0.12	$35/2^+ \rightarrow 31/2^+$
1027.3	8.3±0.8	0.91±0.19	$39/2^+ \rightarrow 35/2^+$
217.4	5.9±0.4	0.93±0.09	$21/2^+ \rightarrow 17/2^+$
402.5	4.1±0.4	0.86±0.04	$25/2^+ \rightarrow 21/2^+$
613.2	8.86±0.7	0.92±0.06	$29/2^+ \rightarrow 25/2^+$
791.2	5.3±0.3	1.17±0.06	$33/2^+ \rightarrow 29/2^+$
931.1	5.1±0.2	0.95±0.12	$37/2^+ \rightarrow 33/2^+$
743.4	20.1±0.9	1.11±0.02	$19/2^+ \rightarrow 15/2^+$
913.2	15.4±0.4	0.91±0.04	$21/2^+ \rightarrow 17/2^+$
Band 5 dipoles (M1/E2)			
677.4	28.1±1.3	0.55±0.04	$17/2^+ \rightarrow 15/2^+$
223.1	20.0±1.1	0.49±0.05	$25/2^+ \rightarrow 23/2^+$
287.7	16.2±0.8	0.47±0.06	$27/2^+ \rightarrow 25/2^+$
370.1	12.1±0.5	0.41±0.05	$31/2^+ \rightarrow 29/2^+$
418.2	9.3±0.7	0.51±0.06	$33/2^+ \rightarrow 31/2^+$
431.3	6.0±0.5	0.59±0.09	$35/2^+ \rightarrow 33/2^+$

Table 4.7: Gamma-ray energies, relative intensities, angular intensity-ratio measurements, spins and parities for the transitions assigned to band 5 where the intensities are given relative to the 508 keV transition of band 1.

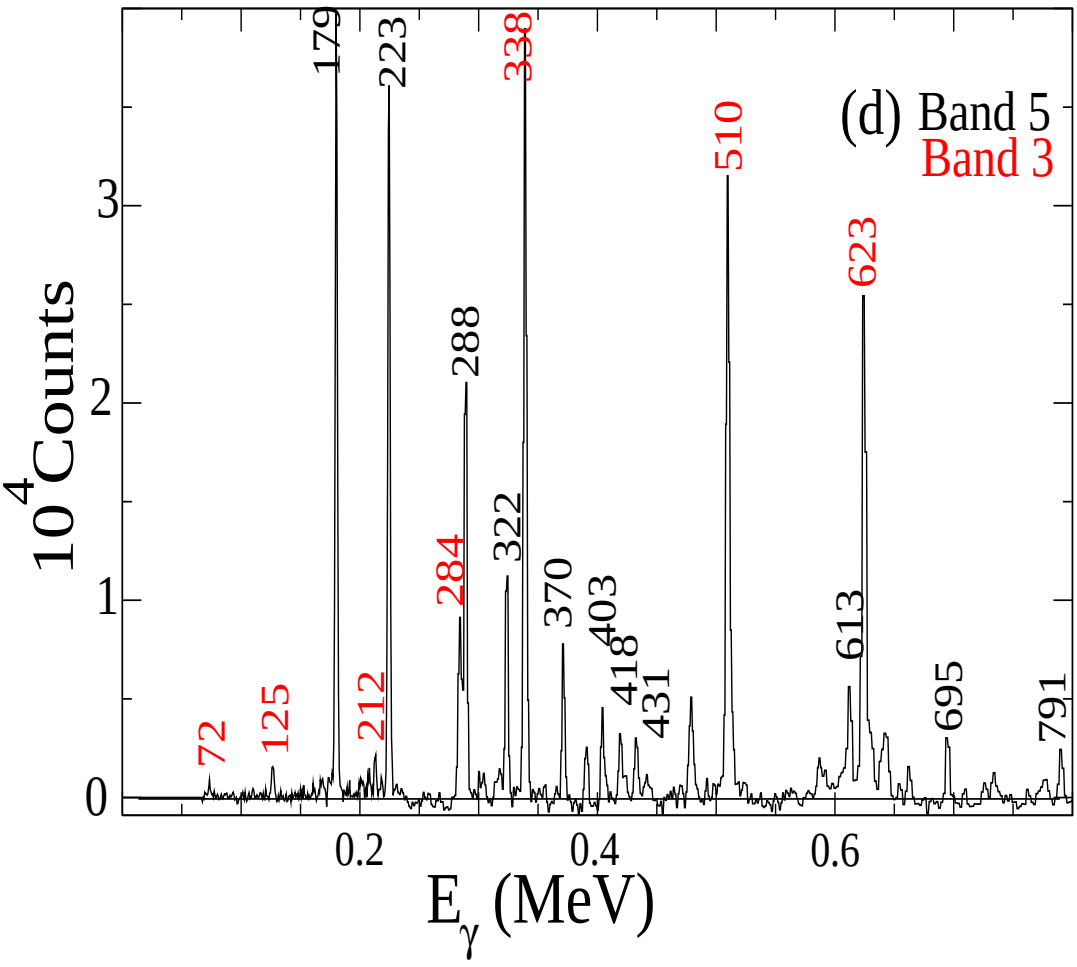

Figure 4.11: The double gated spectrum(x = 152 keV, y = 179 keV) showing band 3 (red) and band 5 (black).

Chapter 5

Discussion

5.1 Introduction

Neutron-deficient nuclei in the light rare earth region $A \sim 130$ with $50 \leq N, Z \leq 82$ have been studied to high spin. These nuclei exhibit a variety of nuclear structure phenomena. The proton and neutron Fermi surfaces lie between the 50 and 82 gaps. Between these gaps there is only the $h_{11/2}$ orbitals for the negative-parity states, whereas there are many positive-parity orbitals which are, namely, $d_{5/2}, g_{7/2}, d_{3/2}$ and $s_{1/2}$. Thus, in the odd-N nuclei in this mass region one can expect the ground state bands and the low lying excited states to be positive parity more than to be negative parity. There are many interesting features in the odd-N nuclei in this mass region, firstly large signature splitting was observed and attributed to the negative triaxial deformation where $\nu h_{11/2}$ orbitals are occupied [41]. The trends of γ-deformation have been investigated and show an increase in γ value from the lightest toward the heaviest nuclei [41, 51]. Moreover, the influence of triaxiality parameter (γ) on the crossing frequencies is greater than the influence of the quadrupole deformation parameter β [39]. Furthermore, the negative parity yrast bands, built on the odd $\nu h_{11/2}$, show the changing of the nuclear shape from triaxial at low spin to prolate at higher spin (after the $\pi h_{11/2}$ crossing) due to the opposite core polarisation effects of $\nu h_{11/2}$ and $\pi h_{11/2}$ orbitals.

Table 5.1: First band-crossing frequencies for the bands 1 and 2 with defined parity and signature (π, α). These values are accurate to ± 0.002 MeV.

^{131}Ce Band	(π, α)	Crossing frequency (MeV/$\hbar$)
1	$(-, -1/2)$	0.329
1	$(-, +1/2)$	0.367
2	$(-, -1/2)$	0.316
2	$(-, +1/2)$	0.316

To obtain the experimental alignments and Routhians, the experimental data must be transformed to the intrinsic frame of the nucleus. This requires the subtraction of the core contribution, leaving the single-particle energy and spin contributions solely. The experimental alignment can be written :

$$i_x(\omega) \quad = \quad I_x(\omega) - I_{x,ref}(\omega). \tag{5.1}$$

The reference term is obtained from the S band of the ^{130}Ce nucleus. At low spin the moment of inertia is proportional to the square of the rotational frequency. Hence the energy reference is based on a variable moment of inertia [52] :

$$\mathcal{J}_{\text{ref}} = \mathcal{J}_0 + \omega^2 \mathcal{J}_1 \tag{5.2}$$

where $\mathcal{J}_0, \mathcal{J}_1$ are Harris parameters [52, 53]. The rotational reference $I_{x,ref}$ is defined by :

$$I_{x,ref}(\omega) \quad = \quad \omega(\mathcal{J}_0 + \omega^2 \mathcal{J}_1). \tag{5.3}$$

where $\mathcal{J}_0 = 17.0\ \hbar^2\ \text{MeV}^{-1}$ and $\mathcal{J}_1 = 25.8\ \hbar^4\ \text{MeV}^{-3}$. The experimental Routhian can be written [52] :

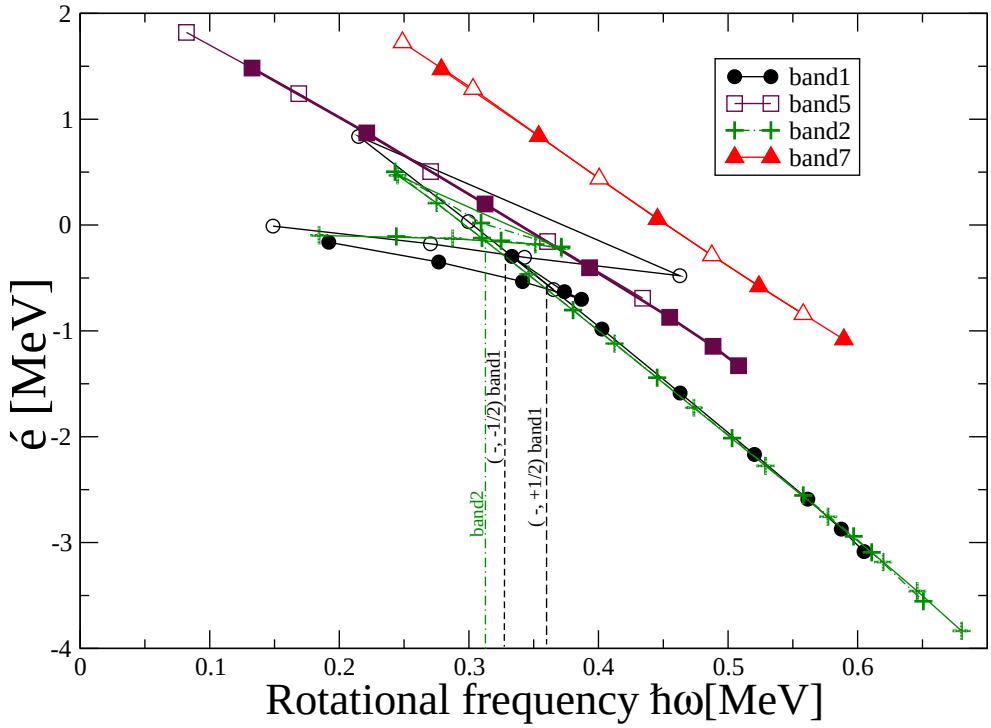

Figure 5.1: Experimental Routhian plot for band 1, 2, 5 and 7. The plot shows first band-crossing frequencies for the bands 1 and 2. Different signature components of the band are marked with full (α= –1/2) and open(α= +1/2) symbols.

Table 5.2: Quasiparticle labelling scheme for ^{131}Ce.

Neutrons			Protons		
Label	Nilsson state	$(\pi,\alpha)_n$	Label	Nilsson state	$(\pi,\alpha)_n$
a	$[404]7/2^+,(g_{7/2})$	$(+,+1/2)_1$	A	$[413]5/2^+,(g_{7/2})$	$(+,+1/2)_1$
b	$[404]7/2^+,(g_{7/2})$	$(+,-1/2)_1$	B	$[413]5/2^+,(g_{7/2})$	$(+,-1/2)_1$
c	$[400]1/2^+,(s_{1/2})$	$(+,+1/2)_2$	C	$[411]3/2^-,(d_{5/2})$	$(+,-1/2)_2$
d	$[400]1/2^+,(s_{1/2})$	$(+,-1/2)_2$	D	$[411]3/2^-,(d_{5/2})$	$(+,+1/2)_2$
e	$[514]9/2^-,(h_{11/2})$	$(-,-1/2)_1$	E	$[550]1/2^-,(h_{11/2})$	$(-,-1/2)_1$
f	$[514]9/2^-,(h_{11/2})$	$(-,+1/2)_1$	F	$[550]1/2^-,(h_{11/2})$	$(-,+1/2)_1$
g	$[541]1/2^-,(h_{9/2})$	$(-,-1/2)_2$	G	$[541]3/2^-,(h_{11/2})$	$(-,-1/2)_2$
h	$[541]1/2^-,(h_{9/2})$	$(-,+1/2)_2$	H	$[541]3/2^-,(h_{11/2})$	$(-,+1/2)_2$

$$e' \;=\; E^{\omega}_{exp}(I) - E^{\omega}_{ref}(I) \tag{5.4}$$

The exact band-crossing frequencies extracted from experimental Routhian Figure 5.1 are summarised in Table 5.1. Woods-Saxon calculations were performed with average deformation parameters $\beta_2 = 0.218, \beta_4 = -0.023$ and $\gamma = 0^o$ which were obtained from total-Routhian surface (TRS) calculations [54, 56]. The Fermi surface for protons lies between $[550]1/2^-$, $[541]3/2^-$ and $[413]5/2^+$ Nilsson states which originate from $h_{11/2}$, $h_{11/2}$ and $g_{7/2}$ orbitals, respectively. Whereas the Fermi surface for neutrons lies near the $[514]9/2^-$, $[404]7/2^+$ and $[541]1/2^-$ Nilsson states which originate from $h_{11/2}$, $g_{7/2}$ and $h_{9/2}$ orbitals, respectively. These states are predominant in terms of assigning configurations. The labelling of the single-particle levels are shown in Table 5.2. Triaxial (γ-soft) nuclear shapes can promote large signature splitting in deformation aligned orbitals at low frequencies. This signature splitting can be interpreted as resulting from triaxial deformation, see section 5.2.1. The staggering parameter has been extracted [70] as a function of spin in order to discuss

the signature splitting, which can be written as :

$$S(I) = E(I) - E(I-1) - \frac{1}{2}\left[E(I+1) - E(I) + E(I-1) - E(I-2)\right]. \quad (5.5)$$

5.2 Interpretation of ^{131}Ce structure

The band structure of ^{131}Ce will be discussed in two sections, corresponding to the negative parity bands and the positive parity bands.

5.2.1 The Negative-parity bands

Band 1

In this band the level structure is built on $11/2^-$ and $9/2^-$ states interpreted to be a coupling between a $h_{11/2}$ neutron hole and a triaxial core [48]. The $9/2^-$ state has been observed to be isomeric, depopulating to the $7/2^+$ state by a 161 keV transition with $T_{1/2} = 80$ ns [48]. This assignment was confirmed in Ref. [47]. The large signature splitting between the signature partners can be seen in Fig 5.2. This signature splitting increases with spin due to the driving force of the $\nu h_{11/2}$ orbital, which polarises the core towards $\gamma < 0$. The TRS calculations performed in Ref. [54] predicted a γ-soft nuclear shape for this band.

It can be seen from Figure 5.3 that this band exhibits a sharp backbend at rotational frequency $\omega \approx 0.3$ MeV/$\hbar$ with a gain in alignment of $\Delta i_x \approx 9\hbar$. By comparing this with the Cranking Shell Model calculations in Figure 5.4, one expects that this gain in alignment is as a result of the alignment of $(\pi h_{11/2})^2$ with no signature splitting (i.e. $\Delta e' \sim 0$ keV) favouring a prolate shape. The staggering parameter has been extracted [70] using Eq. 5.5, in order to discuss the signature splitting. It can be seen in Figure 5.2 that the lower part of this band exhibits a degree of triaxiality ($\gamma < 0$) where the staggering increases with spin up to spin $13\hbar$, then decreases sharply to a minimum value. At spin $25\hbar$, the staggering starts to increase again.

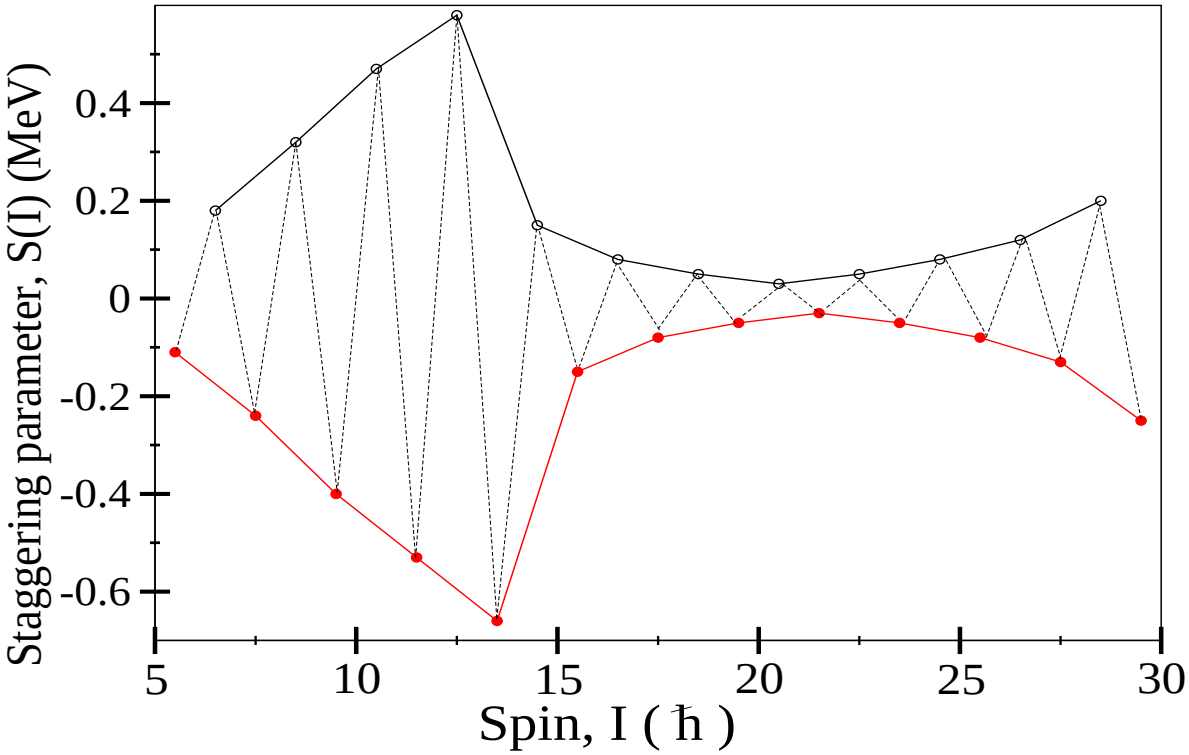

Figure 5.2: Energy staggering parameter S(I) as a function of spin (I) for the negative-parity band 4. Different signature components of the band are marked with full (α= –1/2) and open(α= +1/2) symbols.

Table 5.3: Quasiparticle Configuration regarding to ^{131}Ce.

Band	Quasiparticle Configuration
Band 1	e $\rightarrow$ e $\otimes$ EF
	f $\rightarrow$ f $\otimes$ EF
Band 2	a $\rightarrow$ a $\otimes$ EF
	b $\rightarrow$ b $\otimes$ EF
Band 3	c
	d
Band 4	$\gamma \otimes$ e
	$\gamma \otimes$ f
Band 5	e $\otimes$ AE $\rightarrow$ e $\otimes$ AEFG
	f $\otimes$ AE $\rightarrow$ e $\otimes$ AEFG
Band 6	efg
	feh
Band 7	a $\otimes$ AE
	b $\otimes$ AE

This can be explained at low spin $<13\hbar$ by the driving effect of the $\nu h_{11/2}$ orbital from the upper midshell which drives the nuclear shape away from prolate ($\gamma < 0$). At spin $> 13\hbar$ the rotational alignment of protons from the bottom of the $h_{11/2}$ shell drives the nuclear shape back to prolate ($\gamma = 0$). At higher spin ($25\hbar$) staggering increases again, indicating the shape of the nucleus could be returning to triaxial ($\gamma < 0$) as observed in ^{125,127,129}Ce [43]. The same structures are found in Ba-Nd-Sm nuclei [57, 65]. As shown in Figure 5.3, the alignment i_x remains almost flat after the backbend until $\omega \approx 0.6$ MeV/$\hbar$. At this point the band exhibits a second backbend with a gain in alignment of $\Delta i_x \approx 5\hbar$. This gain in alignment could be interpreted as a two quasiproton crossing (AB). Further experimental data are needed to confirm this.

Band 4

Band 4 is a strongly coupled negative-parity structure with band head spin $15/2^-$. This band is observed at an excitation energy of 972 keV and linked to the yrast band (band 1) by high-energy transitions (994 and 1108 keV). It has the same signature and parity as the yrast band (–,–1/2). A possible interpretation for the configuration of this band is a vibrational excitation coupled to the occupied $\nu h_{11/2}$ in the $[514]9/2^-$ Nilsson orbitals of the yrast band. This configuration assignment is supported by the angular intensity ratio measurements.

Band 6

This negative parity structure is linked to the yrast band by an E2 transition (890 keV). It is interpreted as a three-quasiparticle configuration (efg). It has an intial alignment of $\Delta i_x \approx 5\hbar$. It can be seen from Figure 5.3 that this band has a gain in alignment in the form of an upbend at a rotational frequency $\omega \approx 0.43$ MeV/$\hbar$. This gain in alignment of $\Delta i_x \approx 9\hbar$ is attributed to the (fg) crossing, since the first neutron band crossing (ef) is blocked. This configuration polarises the core even more towards an oblate shape. A similar crossing between a one-quasiparticle $\nu h_{11/2}$ and the three-quasiparticle confguration has been found in Xe-Ba-Ce isotopes [51, 66] and in the ^{133}Nd nucleus [67].

Band 7

In this investigation, two strongly coupled signature partners labelled band 7 in Fig.1, have been observed, which feed the $25/2^-$ and $27/2^-$ states in the yrast band. The band head and parity of this band is assigned based on the angular intensity ratio measurements of the linking transitions, which show that the 950 keV transition is an E2 and the 834 keV transitions is a dipole (M1/E2). Thus, the band head spin is $29/2^-$. This band has no signature splitting, as seen in Figure 5.1, and has an initial alignment of $\Delta i_x \approx 7.5\hbar$ which remains flat. It has been assigned as a three-quasiparticle $\nu g_{7/2} \otimes \pi(g_{7/2}h_{11/2})$ configuration (aAE). This has been confirmed by

the B(M1)/B(E2) ratios which will be discussed in section 5.3.

5.2.2 The positive-parity bands

Band 2

This positive-parity structure is built on the occupation of the $\nu g_{7/2}$, [404]7/2$^+$ Nilsson orbital [47, 50]. It has an initial alignment of $\Delta i_x \approx 1\hbar$ (Figure 5.3). This band exhibits a sharp backbend at rotational frequency $\omega \approx 0.3$ MeV/$\hbar$ with again in alignment of $\Delta i_x \approx 9\hbar$. This can be interpreted as the alignment of $(h_{11/2})^2$ protons in the Nilsson state [550]1/2$^-$ (EF). This configuration is supported by the CSM calculations, Figure 5.4, where the EF levels interact at $\omega \approx 0.3$ MeV/$\hbar$. B(M1)/B(E2) ratios have been calculated in order to confirm this configuration and will be discussed in section 5.3. This band shows another gain in alignment of $\Delta i_x \approx 2\hbar$ at $\omega \approx 0.6$ MeV/$\hbar$, which could be interpreted as an alignment of two quasiproton crossing (AB). Further experimental data are needed to confirm this.

Band 3

This low-lying band was observed in Ref. [49]. It has band head spin and parity 1/2$^+$ with excitation energy $E_x = 61.8$ keV. A possible interpretation for this band is that it is built on the $\nu s_{1/2}$ [400]1/2$^+$ Nilsson state.

Band 5

This positive-parity band is built on a 15/2$^+$ band head. This spin is confirmed by the angular intensity measurment. It has an initial alignment of $\Delta i_x \approx 7\hbar$, as seen in figure 5.3. This band is interpreted as bieng built on the three-quasiparticle configurations eAE and fAE ($\nu h_{11/2} \otimes \pi(g_{7/2}h_{11/2})$). The band gains an alignment of $\Delta i_x \approx 2.5\hbar$ at $\omega \approx 0.45$ MeV/$\hbar$, which is interpreted as the FG crossing, seen at the same frequency in The CSM calculations (Fig. 5.4). Measured B(M1)/B(E2) ratios are again discussed in section 5.3.

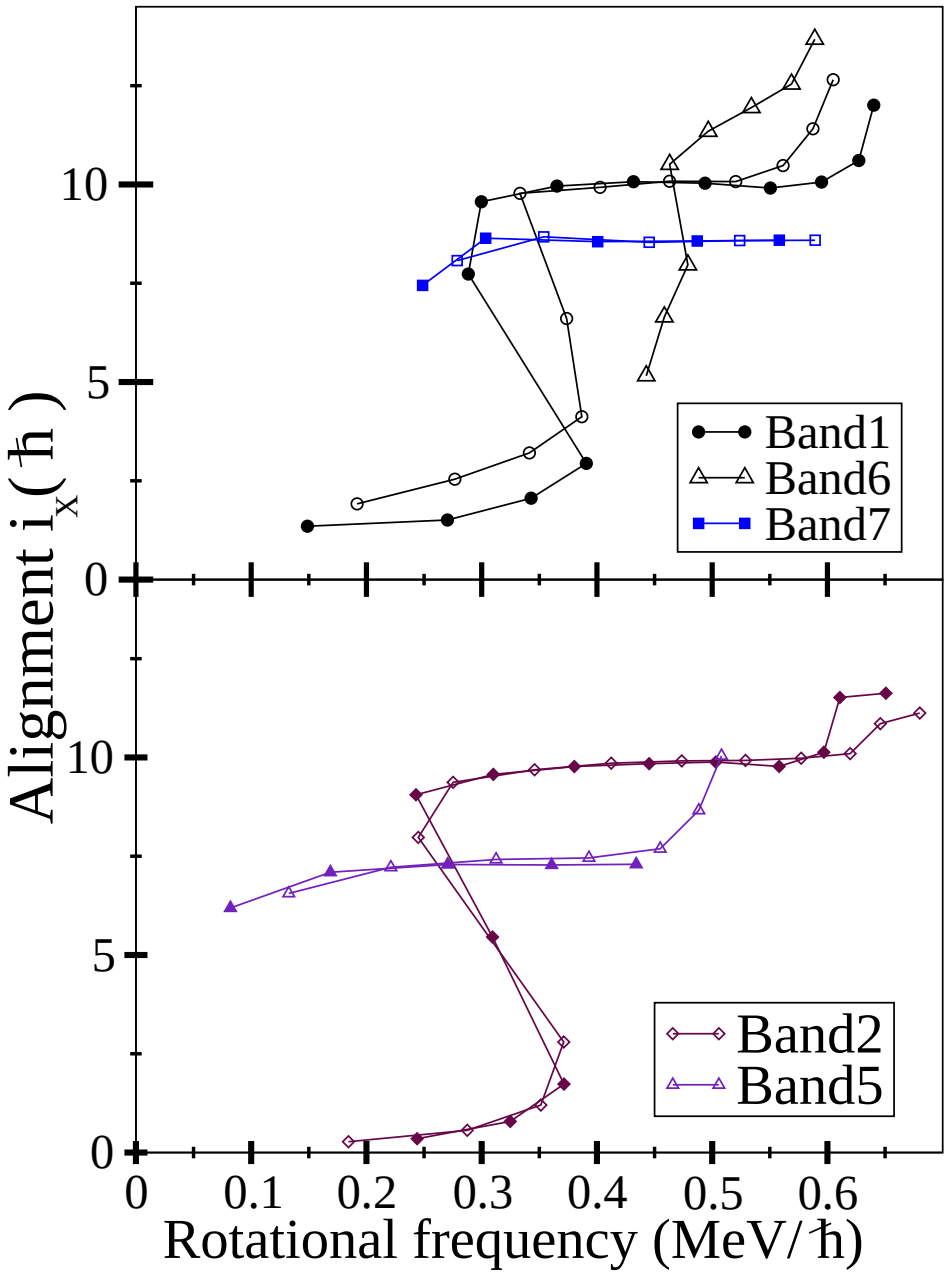

Figure 5.3: The alignment plotted as a function of rotational frequency for all bands. With the Harris parameters $\mathcal{J}_0 = 17.0\ \hbar^2\text{MeV}^{-1}$ and $\mathcal{J}_1 = 25.8\ \hbar^4\text{MeV}^{-3}$. Different signature components of the band are marked with full ($\alpha = -1/2$) and open($\alpha = +1/2$) symbols.

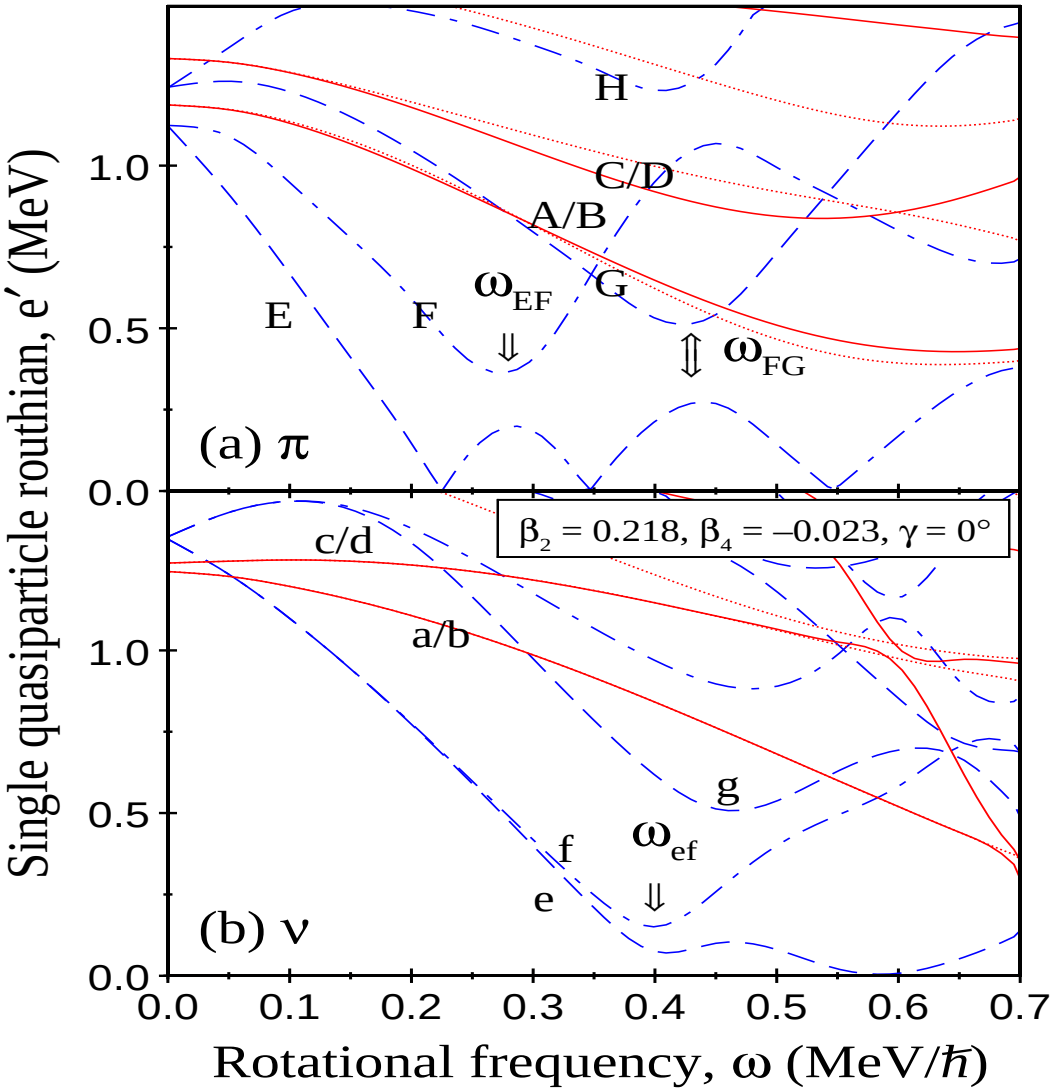

Figure 5.4: Theoretical Woods-Saxon single-partical levels for protons and neutrons as a function of rotational frequency with average deformation parameter $\beta_2 = 0.218$, $\beta_4 = -0.023$ and $\gamma = 0^o$. Solid lines (red) show levels with $(\pi,\alpha) = (+,+1/2)$; dotted lines (red) show $(+,-1/2)$ levels; dashed lines (blue) show $(-,-1/2)$ levels; dot-dashed lines (blue) show $(-,+1/2)$ levels.

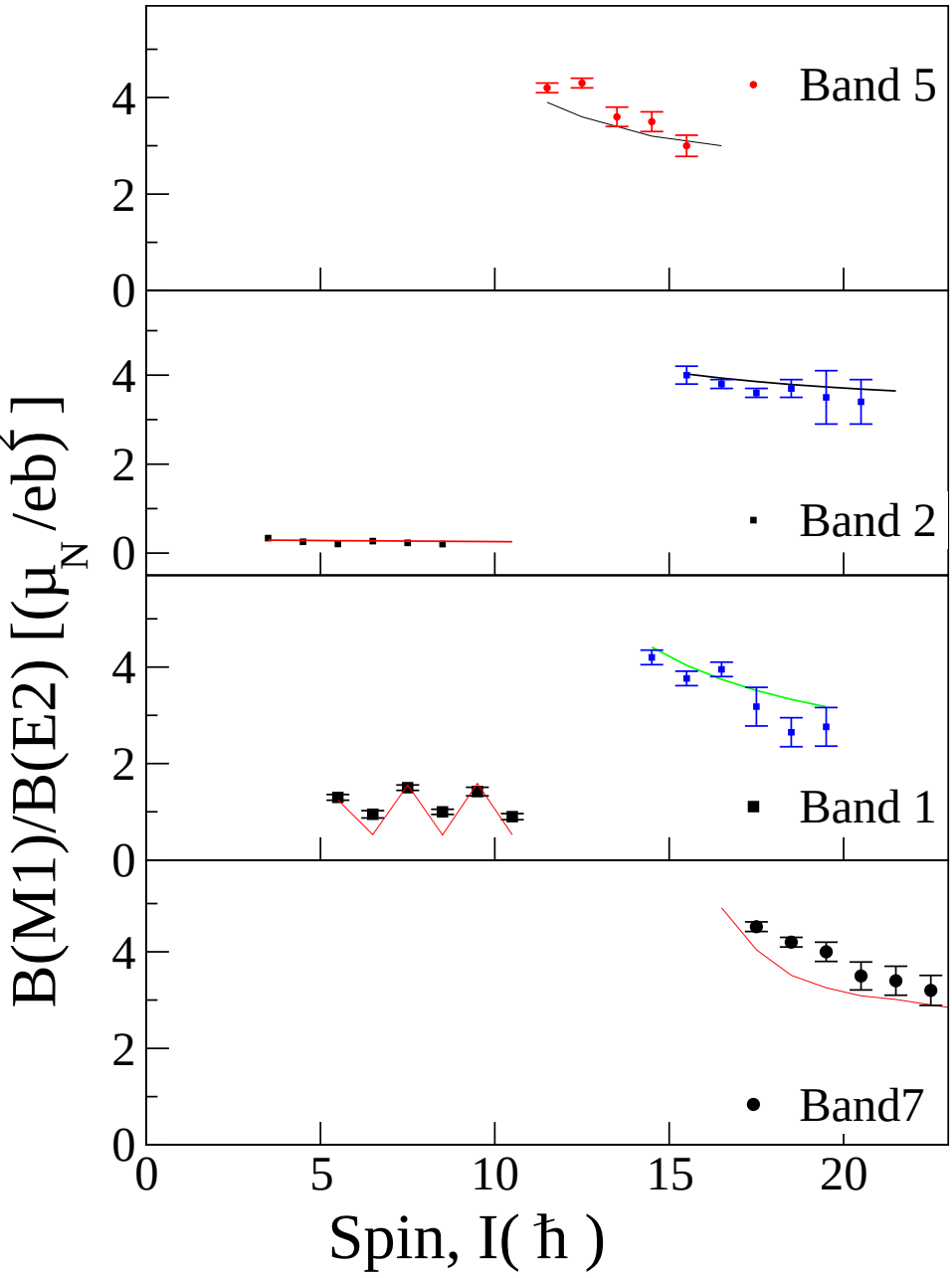

Figure 5.5: The experimental (symbols) and theoretical (lines) of B(M1)/B(E2) ratios for band 1, band 2, band 5 and band 7.

Table 5.4: Values of g-factors and experimental alignments used to calculate the B(M1)/B(E2) ratios of reduced transition probabilities.

Label	Nilsson state	g factor	i_x
Neutrons	$[404]7/2^+$	0.255	0.5
	$[514]9/2^-$	–0.209	2.5
	$[541]1/2^-$	0.209	1.5
Protons	$[413]5/2^+$	0.73	1.5
	$[550]1/2^-$	1.214	4.5

5.3 B(M1)/B(E2) Ratios

The ratios of reduced transition probabilities B(M1)/B(E2) were measured in order to support the assigned configurations. They were calculated using the following equation :

$$\frac{B(M1; I \rightarrow I-1)}{B(E2; I \rightarrow I-2)} = 0.697 \frac{[E_\gamma(I \rightarrow I-2)]^5}{[E_\gamma(I \rightarrow I-1)]^3} \times \frac{1}{\lambda} \frac{1}{[1+\delta^2]} \left[\frac{\mu_N^2}{e^2 b^2}\right], \quad (5.6)$$

where

$$\lambda = I_\gamma(I \rightarrow I-2)/I_\gamma(I \rightarrow I-1) \quad (5.7)$$

and E_γ is measured in MeV. The experimental ratios were extracted from spectra produced by gating above the level of interest, shown in Figure 5.5. The $E2/M1$ multipole mixing ratios were assumed to be zero.

Theoretical calculations of $B(M1)/B(E2)$ were performed using the semi-classical model of Dönau and Frauendorf [68, 69]. The g-factor values, taken from single-particle estimates [71], and the average experimental alignments used are summarised in Table 5.4. The quadrupole moment Q_0 of the core was calculated from the predicted TRS deformation parameter and its g-factor equal to Z/A.

It can be seen in Figure 5.5 that there is a good agreement between experimental and theoretical results, strengthening the suggested configuration assignments. The experimental B(M1)/B(E2) ratios for band 1, which has a signature splitting at low spin ($\Delta e' \sim 130$ keV), show a zigzag pattern in good agreement with the theoretical estimates. There is an increase in B(M1)/B(E2) of band 1 around spin 15 $\hbar$ where the $h_{11/2}$ protons align, and the same is seen for band 2. The empirical B(M1)/B(E2) ratio for band 1 is around 1 $(\mu_N/eb)^2$ at low spin and around 3.5 $(\mu_N/eb)^2$ after the backbend, whereas it is smaller in band 2 (around 0.25 $(\mu_N/eb)^2$) before the backbend and around 4 $(\mu_N/eb)^2$ after the backbend. The ratios is around 3.75 $(\mu_N/eb)^2$ in band 7 which similar to that of band 5.

5.4 Conclusion

High-spin states have been studied in the neutron-deficient odd-N ^{131}Ce nucleus. The experiment was performed at Argonne Laboratory, (USA), using the fusion evaporation reaction ^{100}Mo(^{36}S,5nγ). The beam of ^{36}S was accelerated by Argonne Tandem Linac Accelerator System (ATLAS) to energy of 165 MeV with a beam current of 5 pnA. The gamma ray coincidence data were recorded with GAMMASPHERE.

This detailed spectroscopic study of ^{131}Ce has established two strongly coupled bands, band 4 and band 7. Band 7 is interpreted as a three quasiparticle configuration (a,b $\otimes$ AE) and band 4 is interpreted as a gamma band coupled to a neutron hole $h_{11/2}$. The known bands have been extended to higher spin and in doing so further gains in alignment for bands 1, 2 and 6 have been observed. These gains in alignment are interpreted as a result of the alignment of two quasiproton crossing (AB). Cranked Woods-Saxon calculations have been used to assign possible configurations to the newly found structures. Angular intensity ratio measurements were employed to gain information on the multipolarities of transitions in this nucleus, allowing the spin and parities of the band head of the newly found structures to be deduced and confirming the previous spin/parity assignments for the known bands.

In order to strengthen the configuration assignment suggested in this work and previous work for the ^{131}Ce bands, a comparison of the experimental and theoretical B(M1)/B(E2) ratios was carried out, which showed a good agreement between theoretical and experimental calculations. The large signature splitting in the negative-parity band (band 1) is interpreted as due to a non-axial nuclear shape induced by the core-polarisation effects of neutrons from the upper $h_{11/2}$ midshell.

By comparing ^{131}Ce with other neighbouring odd mass Ce isotopes (^{127,129,133}Ce) there are many interesting features. One of the interesting features is related to the negative-parity yrast bands, built on $\nu h_{11/2}$ orbitals from the upper midshell, which exhibit a large signature splitting. This signature splitting initially increases with spin, then, after the alignment of a proton pair it decreases to almost zero. In these bands it is believed that the $\nu h_{11/2}$ orbitals drive the nuclear shape to triaxial with $\gamma < 0^{\circ}$. Thus, these nuclei exhibit a triaxial shape at low spin. Whereas the proton Fermi surface lies near the $\pi h_{11/2}$ orbitals which favour a prolate shape. Hence, these nuclei show triaxiality at low spin and near axiality at high spin. This deformation is well described by the triaxiality parameter γ, which has a greater influence on the crossing frequency than the quadruple deformation β.

Finally, in these nuclei a general trend that the signature splitting increases with increasing in the number of neutrons. The yrast bands which assigned as (eEF, fEF) configuration were observed in ^{127,129,131,133}Ce. Another 3-quasiparticle configuration (eAE) were observed in lighter ^{127,129}Ce and heavier ^{133}Ce nuclei. Furthermore, analogous structure to band 3 in ^{131}Ce have been identified in ^{133}Ce.

Bibliography

[1] C.F. von Weizsäcker. Z Phys **96** (1935)431.

[2] P. Hodgson, E. Gadioli, E. Gadioli-Erba.*Introductory Nuclear Physics*, Oxford Science Publication, (1997), Page 333.

[3] K. S. Krane, *Introductory Nuclear Physics*, John Wiley Sons (1988).

[4] P. Ring and P. Schuck. *The Nuclear Many-Body Problem*, Springer-Verlag Inc (1980).

[5] R. D. Woods and D. S. Saxon. Physical Review **95** (1954) 577-578.

[6] O. Haxel, J.H.D. Jensen and H.E. Suess. Physical Review **75**(1980) 1766.

[7] M.G. Mayer, Physical Review **95** (1949) 1969.

[8] P. Ring *et al.*, Phys. Lett **B100** (1982) 423.

[9] G. Andersson, *et al.*, Nuclear Physics **A268** (1976) 205.

[10] A. Bohr and B.R. Mottelson. *Nuclear Structure*. W.A. Benjamin Inc (1969).

[11] S. S. M. Wong. *Introductiry Nuclear Physics*, Wiley-VCH (1998).

[12] S.G. Nilsson *et al.*, Nucl. Phys. **A131** (1969) 1.

[13] B. Nilsson. Nucl. Phys. **A129** (1969) 445.

[14] A. Bohr *et al.*, Phys. Rev. **110** (1958) 936.

[15] S. T. Belyaev, Mat. Fys. Medd. Dan. Vid. Selsk. **31** (1959) No.11.

[16] M.G. Mayer, Phys. Rev. **78** (1950) 22.

[17] A. Raymond, Sorensen. Reviews of Modern Physics **45**, No.3, (1973) 353- 377.

[18] A. Bohr and B. Mottelson. Phys. Scr **24** (1981)71-76.

[19] F.S. Stephen, Nucl. Phys. **A183** (1972) 257.

[20] B. Mottelson, and J. Valatin. Physical Review Letters **5**, No. 11, (1960) 511-512.

[21] F. S. Stephens. Reviews of Modern Physics, **47**, No. 1, (1975) 43- 65.

[22] A.Johnson, et al., Physics Letters **B34** (1971) 605608.

[23] E. Grosse, *et al.*, Physical Review Letters **31** (1973) 840.

[24] D. R. Inglis. Particle Derivation of Nuclear Rotation Properties Associatedwith a Surface Wave. Physical Review **96** (1954) 10591065.

[25] D. R. Inglis. Nuclear Moments of Inertia due to Nucleon Motion in a Rotating Well. Physical Review **103** (1956) 17861795.

[26] R. Bengtsson and S. Frauendorf. Nucl. Phys. **A327** (1979) 139-171.

[27] Z. Szymanski, Fast Nuclear Rotation, Claredon Press, Oxford (1983).

[28] P.E. Hodgson. *Nuclear Heavy Ion Reactions*. Oxford Clarendon Press. (1978).

[29] N. Bohr. Nature **137** (1936) 344.

[30] R. Bass. *Nuclear Reactions with Heavy Ions*. Springer-Verlag Berlin (1980).

[31] G.F. Knoll, Radiation Detection and Measurement, Third Edition, Wiley (2000).

[32] M. Devlin *et al.*, Nucl. Instr. Meth.**A383** (1996) 506

[33] I. Y. Lee, Nucl. Phys. **A520**, (1990) 641c.

[34] C. W. Beausang J. Simpson, J. Phys **G22** (1996) 527.

[35] P. J. Nolan*et al.*, Nucl. Instr. Sci (1994) 561-607.

[36] http://nucalf.physics.fsu.edu/ riley/gamma/, *GAMMASPHERE Online Booklet Homepage.*

[37] S. Törmänen *et al.,* Nucl. Phys. **A613** (1997) 282.

[38] E.S. Paul,*Angular correlation analysis with Eurogam II* (1995).

[39] R. Ma, E. S. Paul, C. W. Beausang, S. Shi. N. Xu, and D. B. Fossan, Phys. Rev **C36** (1987).

[40] G. Andersson, S. E. Larsson, G. Leander, P. Möller, S. G. Nilsson, I. Ragnarsson,S. Åberg, R. Bengetsson, J. Dudek, B. Nerlo-Pomorska, K. pomorski, and Z. Szymanski, Nucl. Phys **A268** (1976) 205.

[41] O. Zeidan *et al.,* Phys. Rev **C65** (2002) 024303.

[42] E. S. Paul, C. W. Beausang, D. B. Fossan, R. Ma, W. F. Piel, Jr., N. Xu, L. Hildingsson, and G. A. Leander, Phys. Rev Lett **58**, 984 (1987).

[43] E. S. Paul *et al.,* Phys. Rev **C80** (2009) 054312.

[44] P. J. Nolan, F. A. Beck, and D. B. Fossan Ann. Rev. Nucl. Part. Sci **44** (1994) 561.

[45] D. C. Radford, M. Cromaz, and C. J. Beyer, in *Proceedings of the Nuclear Structure 98 Conference, Gatlinburg, 1998*, edited by C. Baktash (1999 American Institute of PhysicsC481), p.570.

[46] D. C. Radford, Nucl. Instrum. and Methodes Phys. Res **A361** (1995) 297.

[47] M.Palacz *et al.,* Nucl. Phys **A338** (1991) 467-468.

[48] J. Gizon, A. Gizon, Nucl. Phys **A290** (1977) 272-284.

[49] P. J. Nolan *et al.,* Phys. Lett **B108** (1982) 269-273.

[50] J. Gizon *et al.,* Nucl. Phys **A605** (1996) 301-333.

[51] A. Granderath, P.F Mantica, R. Bengtsson, R. Wyss, P. von Brentano, A. Gelberg, and F. Seiffert, Nucl. Phys **A597** (1996) 427.

[52] S. M. Harris, Phys. Rev **B509** (1965) 138.

[53] R. Bengtsson and S. Frauendroof, Nucl. Phys **A327** (1979) 139.

[54] R. Wyss, J. Nyberg, A. Johnson, R. Bengtsson, and W. Nazarewicz,Phys. Lett **B215** (1988) 211.

[55] W. Nazarewicz, G. A. Leander, and J. Dudek,Nucl. Phys **A467** (1987) 437.

[56] W. Nazarewicz, R. Wyss, and A. Johnson,Nucl. Phys **A503** (1989) 285.

[57] J.P. Martin, V. Barci, H. El-Samman, A. Gizon, W. Klamra, B.M. Nyak, F.A. Beck, Th. Byrski, and J.C. Merdinger, Nucl. Phys **A489** (1988) 169.

[58] R. Wyss, F. Lidn, J. Nyberg, A. Johnson, D.J.G. Love, A.H. Nelson, D.W. Banes, J. Simpson, A. Kirwan, and R. Bengtsson, Z. Phys **A330** (1988) 123.

[59] A. Dewald et al., Eur. Phys **A330** (1998) 103.

[60] K. Schiffer, A.P. Byrne, A.M. Baxter, G.D. Dracoulis, and A.E. Stuchbery, Z. Phys.**A336** (1990) 239.

[61] R. Ma, Y. Liang, E.S. Paul, N. Xu, D.B. Fossan, L. Hildingsson, and R.A. Wyss, Phys. Rev **C41** (1990) 717.

[62] K. Hauschild et al., Phys. Rev **C54** (1996) 613.

[63] F. Brandolini et al., Phys. Rev **C60** (1999) 024310.

[64] W.F. Piel, Jr., C.W. Beausang, D.B. Fossan, L. Hildingsson, and E.S. Paul, Phys. Rev **C35** (1987) 959

[65] E.S. Paul, R. Ma, C.W. Beausang, D.B. Fossan, W.F. Piel, Jr., S. Shi, N. Xu, and J.-y. Zhang, Phys. Rev. Lett **61** (1988) 42.

[66] D. Bazzacco et al., Phys. Rev **C58** (1998) 2002–2021.

[67] A.P. Byrne, K. Schiffer, G.D. Dracoulis, B. Fabricius, T. Kibdi, A.E. Stuchbery, and K.P. Lieb, Nucl. Phys **A548** (1992) 131.

[68] F. Dönau and S. Frauendorf, in *Proceedings of the Conference on High Angular Momentum Properties of Nuclei, Oak Ridge, 1982*, edited by N. R.Johnson (Harwood Academic, New York, 1983) p143.

[69] F. Dönau, Nucl. Phys **A471** (1987) 496.

[70] A. J. Kreiner, M. A. J. Mariscotti, C. Baktash, E. der Mateosian, and P. Thiederger,Phys. Rev **C23** (1981) 748.

[71] http://ns.ph.liv.ac.uk/ esp/nuclear/BM1BE2/gfactor.html